Topics in Gravitational-Wave Physics

Thesis by
Pavlin Savov

In Partial Fulfillment of the Requirements
for the Degree of
Doctor of Philosophy

California Institute of Technology
Pasadena, California

2008

(Defense: March 17, 2008)

Contents

List of Figures

List of Tables

Chapter 1

Introduction

While the astrophysics community is on the brink of detecting the first gravitational-wave signal [1, 2, 3], efforts continue to improve the existing detectors and develop new technologies for future-generation detectors. In parallel, the need is rapidly growing for improved analyzes and interpretations of the science data that comes from the detectors. This thesis contributes to these issues with research results related to (i) the design of possible upgrades for the Advanced detectors for the ground-based Laser Interferometer Gravitational-wave Observatory (AdvLIGO) [4, 5, 6, 7] (i.e. for improved versions of the initial LIGO detectors [9, 10]), and (ii) future data analysis techniques for the Laser Interferometer Space Antenna (LISA) [11, 12] (a planned space-based gravitational-wave mission). More specifically:

Currently, an international array of first-generation ground-based, laser-interferometer gravitational-wave detectors (consisting of LIGO, VIRGO [13, 14], GEO600 [15, 16] and TAMA300 [17]) is actively searching for gravitational waves in the frequency band (10 Hz – 10 kHz), with peak sensitivity at a few hundred Hertz. On September the 30th, 2007, the initial LIGO interferometers finished their *Science Run 5* (S5) [18], which collected one-year of triple coincidence data at the interferometers' design sensitivity. The next version of LIGO's interferometers, called Enhanced LIGO [19], with amplitude sensitivity improved by a factor about 2 (event rate increased by a factor $2^3 \simeq 10$), is being implemented and will collect data in science mode in 2009-10. Advanced LIGO is expected to begin operations around 2013. At the end of commissioning, it will have a factor ten better amplitude sensitivity than initial LIGO, which translates to a thousand-fold increase in event rate. Therefore, just a few hours of observations by AdvLIGO will be worth the entire lifetime of initial LIGO. Another significant advantage of the Advanced LIGO design is that it will allow tuning of the sensitivity as a function of frequency, so as to optimize searches for specific astrophysical sources with specific expected spectra.

LISA, the first system of space-based gravitational-wave interferometers, is planned for launch and science operation in 2018 or perhaps somewhat later, depending on political developments. It will operate with peak sensitivity around a few milliHertz and should detect galore of signals simultaneously. The lifetime of the mission is expected to be around five years.

his thesis consists of four chapters: this introductory chapter, two chapters (2 and 3) dealing with research relevant to the technology for a possible upgrade of Advanced LIGO, and one chapter (4) relevant to data analysis for LISA. Specifically: Chapter 2 elucidates the influence of the shape (power profile) of an interferometer's arm-cavity light beams on a *tilt instability*, in which the tilt of an arm cavity mirror is driven by light pressure. Chapter 3 proves a duality relation between arm cavities with almost flat mirrors (as originally planned for AdvLIGO) and cavities with almost concentric spherical mirrors (a design change that has been made, to control the tilt instability). I discovered and used this duality relation numerically in the research reported in Chapter 2, but only later, in collaboration with others, did I prove the duality relation analytically (Chapter 3). Chapter 4 reports details of and results from a Mock LISA Data Challenge in which gravitational wave signals from (mock) supermassive black-hole binaries were sought and found in simulated LISA data.

1.1 Tilt instability in Advanced LIGO: Chapter 2

> Chapter 2, on the tilt instability, is a paper written by me and Prof. Sergey Vyatchanin from the Moscow State University, and published in Physical Review D [20]. Prof. Vyatchanin proposed the theoretical model that we use for evaluating the strength of the instability for nearly flat mirrors with a specific shape: the "Mexican hat". After correcting some minor errors, I extended Vyatchanin's model to non-spherical mirrors with arbitrary shapes, and I developed a numerical solver to evaluate the instability's strength as a function of mirror shape (or, equivalently, of the shape of the cavity's light beam), focusing primarily on Mexican-hat shapes. I then used my numerical solver to derive the results reported in this chapter. I wrote the prose in the paper and I am responsible

for any typos and inaccuracies.

Advanced LIGO is designed to operate near the *standard quantum limit* for displacement measurements. In order to achieve this level of sensitivity, the circulating power inside the optical cavity must be increased from about 10 kW in initial LIGO to almost 1 MW in Advanced LIGO. Unfortunately, such high power will also lead to several types of instabilities, among which an instability due to tilts of the mirrors [21, 22, 23]: We study and calculate the strength of optical-pressure torques in LIGO's Fabry-Perot arm cavity, as a function of the mirror and light-beam shapes. Specifically, we compare analytical and numerical results between cavity configurations with spherical and Mexican-hat mirror shapes that are either nearly flat or nearly concentric. (Advanced LIGO uses nearly flat or nearly concentric mirrors, so as to make the beam spots on the mirrors significantly larger than the diffraction-dictated minimum size; large beams are key to reducing thermal noises — see below. Mexican-hat mirrors have been proposed as a possible upgrade of Advanced LIGO, to reduce thermal noises.)

1.1.1 Tilt instability in optical cavities with spherical mirrors

Braginsky and Manukin [21] were the first to identify the tilt instability and point out that it might be a serious issue in the high-powered arm cavities of AdvLIGO. Sidles and Sigg [22, 23] used a geometric approach to calculate the instability's optical torques for cavities with spherical mirrors. They showed that, when the mirrors are tilted in an antisymmetric way, the resulting torques are stabilizing, but a symmetric tilt destabilizes the mirrors. They also showed that nearly concentric mirror configurations are less unstable than nearly flat configurations with the same diffraction losses, and therefore, are favored for the design of AdvLIGO. Using a geometric approach, Sidles and Sigg calculated the optical-pressure torque on the mirrors, to first-order in tilt angle θ, to be:

$$T = \frac{2PL}{c}\frac{\theta}{(1-g)}, \tag{1.1}$$

where P is the total circulating power, L is the length of the cavity, and g - is the *g-factor* of the cavity ($g = 1 - L/R$, with R the mirrors radius of curvature).

In Section 2.4 we generalize this result using modal analysis and first-order perturbation theory in θ for mirrors with arbitrary shapes. In particular we study cavities with *Mexican-hat* mirrors and the *mesa beams* which they support.

1.1.2 Mexican-hat mirrors and Mesa beams

Mexican-hat mirrors, which support mesa-shaped beams in optical cavities, were proposed by O'Shaughnessy and Thorne [24, 25] as a way to reduce thermoelastic noise in Advanced LIGO. This was in an era when the AdvLIGO baseline design included sapphire substrates for the mirrors, in which thermoelastic noise was severe at the AdvLIGO sweet spot ($f \approx 40 - 200$ Hz). Thermoelastic noise is due to random heat flows in the test masses where cold regions contract and hot regions expand, producing imperfections on the surface of the mirrors. As these imperfections do not cancel completely when averaged over the intensity profile of a Gaussian beam, there is a residual that mimics a signal. This residual could be lowered significantly if the intensity profile of the laser beam is uniformly distributed over the mirror surface. At the same time, the light must be confined towards the center of the mirrors in order to decrease power leakage, so when the uniform distribution ends, the light intensity must decay rapidly toward the edges of the mirrors. O'Shaughnessy and Thorne developed a method to mathematically generate beams that have these properties, called "mesa beams". Because of their shape, the mirrors that support mesa beams are called Mexican-hat mirrors.

More recently, the baseline design for Advanced LIGO has been changed from sapphire to fused-silica substrates, in which thermoelastic noise is less severe, and a number of different thermal noises are of roughly equal importance. Studies by Lovelace and others (see details and references in Lovelace's paper [26]) show that all the thermal noises can be reduced significantly by switching from spherical mirrors with their Gaussian beams to Mexican-hat mirrors with their Mesa beams, so the study in Chap 2 of the tilt instability for spherical and Mexican-hat mirrors remains important for the new baseline, as it was for the old.

Also more recently, Bondarescu and Chen [27] and others [28, 29] have conceived new mirror shapes that reduce thermal noises even more than Mexican-hat mirrors. Studies of the tilt instability are currently being performed for these new shapes [30].

1.1.3 Tilt Instability in optical cavities with Mexican-hat mirrors

Because cavities with nearly concentric mirrors are much less unstable under tilt than cavities with nearly flat mirrors, and Mexican-hat mirrors reduce thermal noise, it looks like the optimal combination would be a cavity with nearly concentric Mexican-hat mirrors. Thorne [31] suggested a method to mathematically design this kind of mirror by propagating concentric Gaussian beams and matching their wave-fronts. In Chapter 2 we develop a numerical scheme to implement this (and many other) mirrors shapes, and solve for the eigenmodes of the cavities. The properties of the mirrors and the supported beams are described in Section 2.5. We also resolve analytically the eigenmodes of the perturbed (tilted-mirror) cavities and calculate the optical torques induced by tilt. We compare our results to well-known theoretical results and those of Sidles and Sigg for cavities with spherical mirrors and we show that nearly flat Mexican-hat mirrors are significantly more unstable to tilt than nearly concentric Mexican-hat mirrors, and spherical mirrors, both nearly flat and nearly concentric. We conclude that optical cavities with nearly concentric Mexican-hat mirrors not only have thermoelastic noise lower by a factor of 3 than the corresponding spherical mirrors; they are also less unstable to tilt. In other words: of all the mirrors we consider, the nearly concentric Mexican-hat ones have the best thermal noise and tilt instability performance.

1.2 A duality relation between non-spherical optical cavities: Chapter 3

> Chapter 3 is a paper by Juri Agresti, Yanbei Chen, Erika D'Ambrosio, and me, which has been submitted to Physical Review D. A pre-print of the paper is available in the arXiv database [32]. I discovered the duality relation numerically in my studies of higher order modes of cavities with Mexican-hat mirrors. In further numerical explorations, I saw the duality and discovered its details for the eigenspectra of cavities with arbitrarily shaped mirrors. Based on this numerical work, in the paper that constitutes Chap. 2 of this thesis, I formulated this duality relation as a conjecture. Chapter 3 gives two analytic proofs of my duality relation. Yanbei Chen proposed the idea behind one of the proofs, based on the cavity's center-to-center propagator. I worked out the full details of the

proof and Chen and I together wrote the prose in Sections 3.1, 3.3, and 3.5. Independently, Juri Agresti and Erika D'Ambrosio from the LIGO Laboratory at Caltech carried out the other proof based on properties of the mirror-to-mirror propagator. They wrote the text in Sections 3.2 and 3.4.

As part of my study of the tilt instability in optical cavities, my analysis of resonating, higher-order optical modes showed a unique one-to-one mapping between the eigenstates and the eigenvalues of cavities with nearly flat and those with nearly spherical, concentric mirrors — when the deviations from flatness in the one case, and concentric sphericity in the other are identical but of opposite sign. I first saw the mapping when the deviations from flatness or concentric sphericity had the O'Shaugnessy-Thorne Mexican-hat shape. At first, it appeared that the mapping was a property of these specific types of mirrors, as their shapes were constructed mathematically in a very special way: by propagating parallel or concentric Gaussian beams. However, a deeper investigation showed me that the mapping holds for any *dual* cavities — i.e., pairs of cavities whose mirrors have arbitrary (not necessary small), identical but sign-reversed deviations from flatness and concentric spheres. In Chap. 2, I expressed the mapping I discovered as the following conjecture:

1.2.1 Conjecture

If a symmetric, optical cavity has mirrors that deviate from flatness by the axisymmetric height function height $h(|\vec{r}\,|)$, its *dual cavity* has mirrors that deviate from concentric spheres by $-h(|\vec{r}\,|)$. Or equivalently,

$$h^F(|\vec{r}\,|) + h^C(|\vec{r}\,|) = r^2/2R = r^2/L, \tag{1.2}$$

where L is the length of the cavity, and $R = L/2$ is the radius of curvature of the concentric, spherical mirrors. The subscripts F and C stand for the deviating-from-*flat* and deviating-from-*concentric* cavity configurations respectively. I conjectured that dual cavities support eigenmodes which have the same intensity profiles evaluated at the mirrors

$$|u^F_{nm}|^2 = |u^C_{nm}|^2, \tag{1.3}$$

and that their eigenvalues are related by the following formula:

$$\lambda^F_{nm} = (-1)^{m+1}(\lambda^C_{nm})^*, \tag{1.4}$$

for any mode labeled by a pair of integers $n, m = 0, 1, 2, \ldots$, and parity $(-1)^m$.

This duality relation is important for Advanced LIGO because of the recent baseline change from nearly flat to nearly spherical mirrors. Any proposed mirror configuration (e.g. Mexican-hat [24, 25] or Bessel-Gaussian [27]) in the nearly flat regime has a dual configuration in the nearly concentric-spherical regime, whose eigenmodes are the same (aside from the above minor changes), and whose thermal noises will be the same (because of identical intensity profiles), but whose tilt instability will be very different.

1.2.2 Analytical proof, generalization and applications

In Chapter 3 (with colleagues) I prove my conjecture analytically, and we also derive formulas for the mapping between the complex optical fields of the dual cavities, both on the surfaces of the mirrors and at the centers of the cavities.

In Chapter 3, we present two proofs of my duality relation. The first proof was motivated by the method used to construct, mathematically, the Mexican-hat mirrors. Specifically, the generation of an arbitrary, nearly flat cavity configuration involves a *spatial translation* of superposed Gaussian beams, whereas the nearly concentric-spherical configuration involves a *rotation* of the superposed Gaussian beams, or equivalently, translation in momentum $\vec{k}$-space. The fact that the position and momentum space in quantum mechanics are related by a *Fourier transform* helped us show that the eigenequations which describe the propagation of light inside the two dual cavities are connected by a similar two-dimensional *Fourier transform*, and this led to the duality relations (1.3) and (1.4). The second proof in Chapter 3 is based on simple geometric considerations and the properties of the operator that propagates the light from mirror to mirror. In Chap. 3 we also present a detailed derivation of the optical fields in the case of Mexican-hat mirrors and some applications of my duality relation to possible upgrades for Advanced-LIGO design.

1.3 Grid-based search for supermassive black-hole binaries in simulated LISA data: Chapter 4

> The text in Chapter 4 was written by me, as input for a joint paper by a JPL/Caltech group working on Mock LISA Data Challenges (MLDC). The other authors of the joint paper will be Jeff Crowder, Curt Cutler, Ilya Mandel, and Michele Vallisneri. My responsibility in our joint project was to improve and build on the second stage of our group's three-stage wave-search pipeline. I wrote the code for parallel supercomputer structures for our *grid-based* search in the MLDC data. I implemented into the second stage of the pipeline the F-statistics tools (written by C. Cutler and M. Vallisneri) and the sky-map discretization grid (written by me). This second stage of the pipeline was originally designed to use initial data from the first stage (the time-frequency analysis) and to pass the results to a final, third stage (a Markov-Chain-Monte-Carlo search). The code I wrote achieves its goals as the second stage of this three-stage pipeline, and it can also be used as a standalone search method for supermassive black-hole (SMBH) binaries in the LISA data — as I show in Chapter 4.

The Laser Interferometer Space Antenna (LISA), a proposed joint NASA / ESA space mission, is designed to study the universe using gravitational waves in the $(10^{-5} - 10^{-1})$ Hz range [33]. LISA's raw science output will be time series consisting of a large number $(\approx 10^4)$ of resolvable overlapping sources, ranging from galactic stellar- mass binary systems to high-redshift supermassive black holes.

LISA has the potential of discovering new classes of sources, such as GW primordial stochastic backgrounds, cosmic strings and exotic compact objects [34]. Most sources detectable by LISA are long lived compared to the mission lifetime (> 3 yr), and the data will contain strong GW foregrounds generated by abundant populations of galactic and extra-galactic white-dwarf binary systems and possibly stellar-mass compact objects (white dwarfs, neutron stars, and black holes) slowly spiraling into massive black holes in galactic nuclei. Some of the gravitational wave signals (such as waves from these "extreme mass-ratio inspirals") are very complex functions of their sources' physical parameters; others (such as those from Galactic white-dwarf binaries) are simpler, but their resolution will be confused by the presence of many other similar signals overlapping in frequency space.

Although much experience has been gained in the analysis of GW data collected by ground-based detectors, that effort has not taught us anything about how to deal with many overlapping sources. This is because, in the ~ 100 Hz band of ground-based observations, signals are expected to be rare and weak, whereas in LISA's ~ 0.001 Hz band we expect numerous overlapping sources, some with high signal-to-noise ratios (SNR). This difference makes it important, as a preparation for the LISA mission, to tackle the new data analysis problems that arise from overlapping sources.

1.3.1 The Mock LISA Data Challenge

The Mock LISA Data Challenge [35, 36] is a program to encourage the development of new methods of data analysis for LISA. It was organized under the auspices of the LISA International Science Team's Working Group on Data Analysis. Each round of challenges consists of several data sets containing simulated instrument noise and gravitational-wave signals from sources with undisclosed parameters. Participants are asked to analyze the data sets, report their best parameter estimates and describe their search methods. The results are then compiled and compared to the true parameters. The challenges are being released from JPL in rounds of increasing complexity and realism. They are organized by gravitational-wave source type, including the following source classes: Binaries of neutron stars, white dwarfs, ordinary stars, or black holes in our Galaxy; massive black hole (MBH) mergers occurring where distant galaxies have interacted; and extreme mass ratio inspirals (EMRIs), in which a stellar-mass compact object spirals into a massive black hole at the center of a distant galaxy.

1.3.2 A Three-stage search for supermassive black hole binaries in MLDC

The JPL/Caltech group has developed a pipeline to search for inspiriling supermassive black-hole (SMBH) binaries in the MLDC. I am member of the group and have worked on Challenge 2, issued in January 2007 with results due at the end of June 2007, and Challenge 1B, issued in August 2007 and due in December 2007. Our pipeline consists of three stages. The first stage uses a time-frequency track-search method to search for inspiral signals and provide a coarse estimate of the black-hole masses m_1, m_2 and of the coalescence time of the binary t_c. The second stage uses a simultaneous matched-filtering search in the parameter space of the masses (m_1, m_2), the sky-position (θ, ϕ), and the coalescence time t_c. By using the F-statistic, discussed in Section 4.3, we automatically extremize the log likelihood over the five extrinsic parameters of the binary. Finally, the third stage is a Markov-Chain-Monte-Carlo (MCMC) search used to estimate all nine physical parameters of the binary with higher accuracy. To reduce convergence times, the pipeline is designed so that in the last two stages, the search in the multi-parameter space starts from a point determined from the previous stage.

The results discussed in Chapter 4 are from the grid-based search alone. In all seven data sets, the search converges to the key parameters. As the results show, the grid-based search is capable, without any initial data for the parameters, to resolve the signal. However, in the future, it will probably be used to pass the parameter estimates as initial data to the MCMC search which is a superior method when searching in a neighborhood of the true parameters.

Detailed overview and results from the individual challenges can be found in the arXiv database [37, 38] and the MLDC official web site [39].

Bibliography

[1] V. Kalogera, K. Belczynski, C. Kim, R. O'Shaughnessy, and B. Willems *Physics Reports, Hans Bethe Centennial Volume*, **442**, 75,(2007).

[2] A. Vecchio Phys. Rev. D**70**, 042001 (2004).

[3] L. Barack, T. Creighton, C. Cutler, J. Gair, S. Larson, E. Phinney, K. Thorne, and M. Vallisneri (2003), URL `http://www.tapir.caltech.edu/listwg1/EMRI/LISTEMRIreport.pdf`.

[4] E. Gustafson, D. Shoemaker, K.A. Strain, and R. Weiss, "LSC white paper on detector research and development", URL `www.ligo.caltech.edu/docs/T/T990080-00.pdf`.

[5] P. Fritschel (2003), `gr-qc/0308090`.

[6] D. Shoemaker, "Advanced LIGO: Context and Overview (Proposal to the NSF)" (2003), URL `http://www.ligo.caltech.edu/docs/M/M060056-08/M060056-08.pdf`.

[7] Advanced LIGO URL `http://www.ligo.caltech.edu/advLIGO/`.

[8] Advanced LIGO: context and summary URL `http://www.ligo.caltech.edu/advLIGO/scripts/summary.shtml`.

[9] B. Barish and R. Weiss Physics Today**10**, 44 (1999).

[10] A. Abramovici et al., Science **256**, 325 (1992).

[11] P. Bender *et al.*, *LISA Pre-Phase A Report* (1998).

[12] K. Danzman, *et al.*, *LISA – Laser Interferometer Space Antenna, Pre-Phase A Report*, Max-Planck-Institute für Quantenoptic, Report MPQ 233 (1998).

[13] B. Caron et al., Class. Quant. Grav. **14**, 1461 (1997).

[14] F. Acernese, *et al.* Class. Quant. Grav. **23**, S635 (2006).

[15] H. Lück et al., Class. Quant, Grav. **14**, 1471 (1997).

[16] B. Willke et al., Class. Quant, Grav. **19**, 1377 (2002).

[17] M. Ando et al., Phys. Rev. Lett. **86**, 3950 (2001).

[18] "The Latest News from the LIGO Laboratory" (2008), URL `http://www.ligo.caltech.edu/~ll_news/s5_news/s5article.htm`.

[19] R. Adhikari, P. Fritschel, S. Waldman, "Enhanced LIGO", URL `http://docuserv.ligo.caltech.edu/docs/T/T060156-01.pdf` .

[20] P. Savov and S. Vyatchanin, Phys. Rev. D**74**, 082002 (2006).

[21] V. Braginsky and A. Manukin, *Measurement of weak forces in Physics Experiments*, (University of Chicago Press, 1977), pp. 25-39.

[22] D. Sigg, "Angular Instability in High Power FP Cavities" (2003), URL `http://www.ligo.caltech.edu/docs/T/T030120-00.pdf`.

[23] J. Sidles and D. Sigg, "Optical Torques in Suspended Fabry-Perot Interferometers", Phys. Lett. A **354**, 167 (2006).

[24] E. d'Ambrosio, R. O'Shaughnessy, S. Strigin, K.Thorne, and S. Vyatchanin, "Reducing Thermoelastic Noise in Gravitational-Wave Interferometers by Flattening the Light Beams", Phys. Rev. D, (submitted) `gr-qc/0409075`.

[25] E. D'Ambrosio, R. O'Shaughnessy, S. Strigin, K. Thorne, and S. Vyatchanin, "Status Report on Mexican-Hat Flat-Topped Beams for Advanced LIGO" (2003), URL `http://docuserv.ligo.caltech.edu/docs/T/T030009-00.pdf`.

[26] G. Lovelace, Class. Quant. Grav. **24** 4491 (2007).

[27] M. Bondarescu and Y. Chen, (in preparation).

[28] J. Zhi-Ping, Optics Comm., **125** 207 (1995).

[29] P. Adamson, Optics Comm., **88**, 242 (1999).

[30] Y. Chen, (private communication).

[31] K. Thorne, (private communication).

[32] J. Agresti, Y. Chen, E. D'Ambrosio, and P. Savov, Phys. Rev. D (submited) (2005), `gr-qc/0511062`.

[33] P. Bender *et al.*, *LISA Pre-Phase A Report*, (1998).

[34] S. Hughes, Class. Quant. Grav. (submited) (2007), `gr-qc/0711.0188v1` .

[35] K. Arnaud *et al.* (Mock LISA Data Challenge Task Force) 2006. In *Laser Interferometer Space Antenna, Sixth International LISA Symposium* AIP Conf. Proc. 873, ed. Merkowitz S M and Livas J C p 619.

[36] K. Arnaud *et al.* (Mock LISA Data Challenge Task Force) 2006. In *Laser Interferometer Space Antenna, Sixth International LISA Symposium* AIP Conf. Proc. 873, ed. Merkowitz S M and Livas J C p 625.

[37] K. Arnaud *et al.* (Mock LISA Data Challenge Team) (2007), In this volume, gr-qc/0701139.

[38] K. Arnaud *et al.* (Mock LISA Data Challenge Task Force) (2007), In this volume, gr-qc/0701170.

[39] Mock LISA Data Challenge URL `http://astrogravs.nasa.gov/docs/mldc/`.

[40] D. Brown, J. Crowder, C. Cutler, I. Mandel, M. Vallisneri, Class. Quant. Grav., (submitted) `arXiv:0704.2447`.

Chapter 2

Tilt Instability of Mesa-Beam and Gaussian-Beam Modes for Advanced LIGO

Sidles and Sigg have shown that advanced LIGO interferometers will encounter a serious *tilt instability*, in which symmetric tilts of the mirrors of an arm cavity cause the cavity's light beam to slide sideways, so its radiation pressure exerts a torque that increases the tilt. Sidles and Sigg showed that the strength T of this torque is 26.2 times greater for advanced LIGO's baseline cavities — nearly *flat* spherical mirrors which support *Gaussian* beams ("FG" cavities), than for nearly *concentric* spherical mirrors which support Gaussian beams ("CG" cavities) with the same diffraction losses as the baseline case: $T^{FG}/T^{CG} = 26.2$. This has motivated a proposal to change the baseline design to nearly concentric, spherical mirrors. In order to reduce thermal noises in advanced LIGO, O'Shaughnessy and Thorne have proposed replacing the spherical mirrors and their Gaussian beams by "Mexican-Hat" (MH) shaped mirrors which support flat-topped, "mesa" shaped beams. In this paper, we compute the tilt-instability torque for advanced-LIGO cavities with nearly flat MH mirrors and mesa beams ("FM" cavities) and nearly concentric MH mirrors and mesa beams ("CM" cavities), with the same diffraction losses as in the baseline FG case. We find that the relative sizes of the restoring torques are $T^{CM}/T^{CG} = 0.91$, $T^{FM}/T^{CG} = 96$, $T^{FM}/T^{FG} = 3.67$. Thus, the nearly concentric MH mirrors have a weaker tilt instability than any other configuration. Their thermoelastic noise is the same as for nearly flat MH mirrors, and is much lower than for spherical mirrors.

2.1 Introduction

Thermal noises in mirror substrates and mirror coatings are the dominant noise sources for advanced LIGO at and somewhat below the frequency of optimal sensitivity. When sapphire mirrors were planned for advanced LIGO, the dominant thermal noise was thermoelastic substrate noise, and O'Shaughessy and Thorne [1, 2] proposed lowering that noise by flattening the cross-sectional profile of the arm cavities' light beams — i.e., by replacing the standard Gaussian-shaped beams by "mesa"-shaped beams (thick curves in Fig. 2.2 below). This can be achieved by replacing LIGO's nearly flat, spherically shaped mirrors by mirrors that have a nearly flat "Mexican-hat" (MH) shape. More recently, fused silica has been selected as baseline mirror material, and thermoelastic substrate noise is no longer dominant. However, the other three forms of thermal noise (Brownian substrate, Brownian coating, and thermoelastic coating) are also substantially reduced by switching from Gaussian beams and spherical mirrors to mesa beams and Mexican-hat mirrors, so mesa beams remain an attractive possibility for advanced LIGO and/or for other future interferometers. For detailed computations of the noise reductions achieved by using mesa beams, see O'Shaughessy, Strigin and Vyatchanin [1, 2, 3], Agresti [4, 5, 6] and Lovelace [7].

Sidles and Sigg[8, 9] have recently rediscovered a *tilt instability* in Fabry-Perot (FP) cavities, first pointed out by Braginsky and Manukin [10], and they have shown that this instability is a serious issue for advanced LIGO's arm cavities, because of their high circulating light power (about 800 kW) and resulting high light pressure. In this instability, random forces cause the cavity's mirrors to tilt in a symmetric way[1] (Fig. 2.1b), and this tilt causes the light beam to slide sideways in the cavity by the distance $\delta x_{\rm sym}$ shown in the figure, so its light pressure exerts a torque T on the mirrors that tries to increase their tilt. [Sidles and Sigg also showed that, when the mirrors are tilted in an antisymmetric way as in Fig. 2.1c, the resulting torque is stabilizing rather than destabilizing.] Sidles and Sigg analyzed the tilt instability, using geometric arguments, for cavities with nearly *flat*, spherical mirrors and their *Gaussian* light beams ("FG" cavities), and also for nearly

---

[1] Sidles and Sigg [8, 9] use the opposite convention from us for "symmetric and "antisymmetric" tilt.

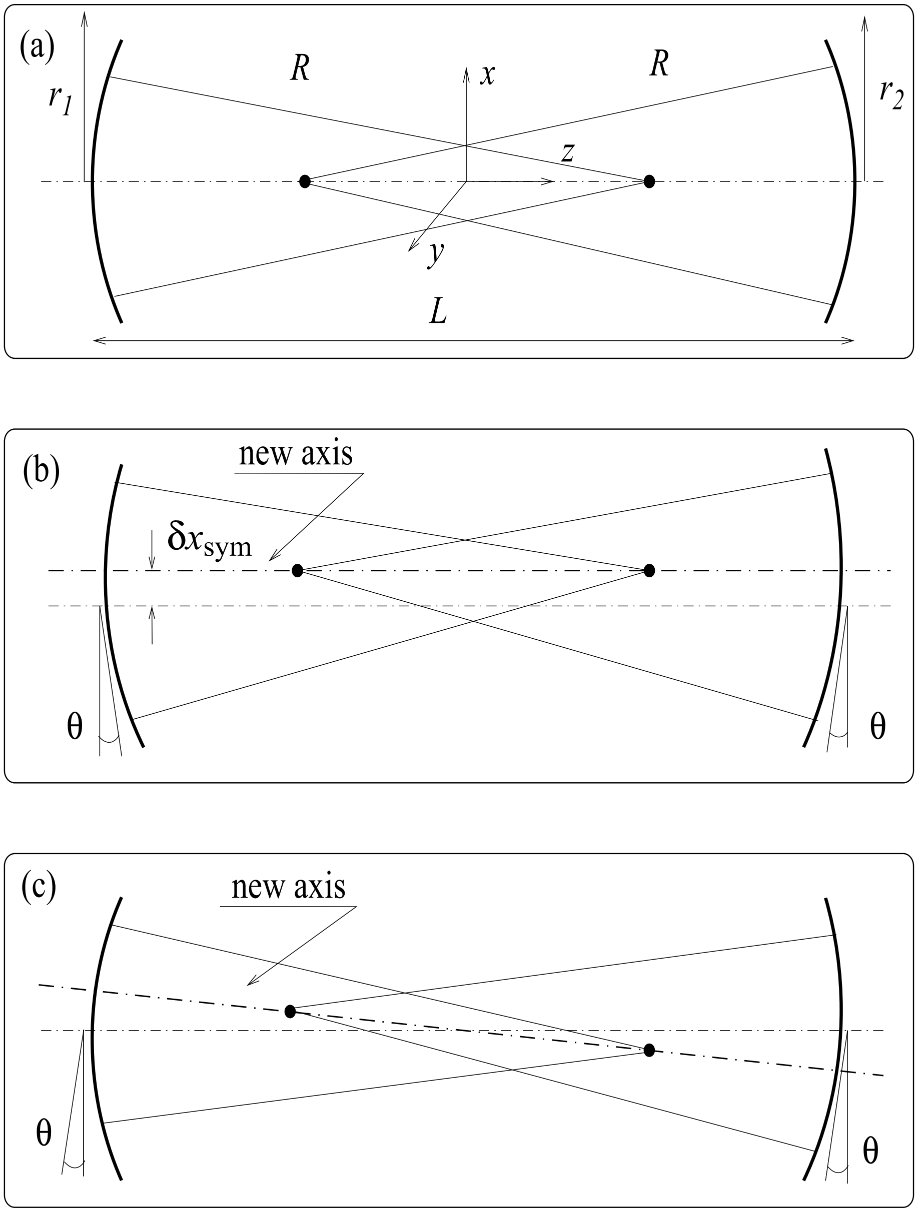

Figure 2.1: Horizontal section of FP resonator with (a) perfectly positioned spherical mirrors, (b) symmetrically tilted spherical mirrors and (c) antisymmetrically tilted spherical mirrors

concentric, spherical mirrors and their Gaussian beams ("CG" cavities). [The mirrors must be nearly flat or nearly concentric in order to make the light beams significantly larger than the Fresnel diffraction size, $b = \sqrt{\lambda L/2\pi}$ with λ the light's wavelength and L the cavity length; large beams are required to keep the thermoelastic noise small.] Sidles and Sigg found that the instability is much more severe for the baseline FG cavities than for CG cavities with the same beam radii at the mirrors and thence the same diffraction losses. On this basis, the baseline design for advanced LIGO [11] has been changed from FG cavities with nearly flat mirrors to CG cavities with nearly concentric mirrors.

Motivated by this Sidles-Sigg work, Thorne has proposed a mathematical way to design nearly concentric MH mirrors that support mesa beams with precisely the same mesa-shaped light-power distributions on the mirrors as for the original nearly flat MH mirrors. Thorne's mathematical construction is presented, along with some generalizations of it, in a companion paper by Bondarescu [12].

In the present paper, we analyze the tilt instability for advanced-LIGO arm cavities with (i) nearly flat MH mirrors and their mesa beams ("FM" cavities), and (ii) with Thorne's new nearly concentric MH mirrors and their mesa beams ("CM" cavities). We employ first-order perturbation theory in our analysis, by contrast with the Sidles-Sigg geometric techniques. We compare the strength of the tilt's destabilizing torque T for FG, FM, CG, and CM cavities that have beam sizes chosen so they all have the same diffraction losses, about 20 ppm; and we explore two choices for the radius of the mirror coating on the substrates: the baseline radius (14.7 cm), and a larger coated radius (16 cm) used in the analysis of d'Ambrosio et. al. [1, 2] [their *fiducial* configuration].

In our numerical solutions to the eigenequation for the light's eigenmodes inside FM and CM cavities, we discovered remarkable *duality relations* between cavities with axisymmetric mirrors that deviate by an amount $H(r)$ from flatness, and cavities with mirrors that deviate by $-H(r)$ from concentric spheres. We verified these numerically discovered duality relations for several different forms of $H(r)$, in addition to those of MH mirrors. This motivated Chen and Savov, and independently Agresti and d'Ambrosio [13] to devise analytic proofs of our duality relations. The duality relations provide a unique one-to-one mapping between the eigenstates and eigenvalues of the dual cavities — a mapping that may be useful not only for advanced LIGO but in a variety of other applications of Fabry Perot cavities.

This paper is organized as follows. In Sec. II, we use a first-order modal analysis of a Fabry-Perot cavity to derive a general formula for the torque exerted on the mirrors when the cavity is perturbed, in terms of as-yet unknown mode coupling coefficients α_k and mode-overlap integrals I_k. In Sec. III, we use first-order perturbation theory of Gaussian-beam (FG and CG) cavities to derive analytical formulas for α_k and I_k, and thence for the tilt-induced torque T in the FG and CG cases, and we show that our formula for the torque is equivalent to that of Sidles and Sigg [8, 9]. In Sec. IV we use first-order perturbation theory to derive formulas for the coupling coefficients α_k, and thence for the torque T, in terms of a cavity's eigenvalues and mode-overlap integrals I_k. In Sec. V we present our numerical results for the modes and their eigenvalues for FM, CM, FG, and CG cavities, and we discuss the duality relations between the nearly flat and nearly concentric cases. Finally, in Sec. VI, we combine the numerical results of Sec. V with the formulas of Secs. III and IV, to deduce the tilt-induced torque for our four cavity designs — using two sets of parameters: those for cavities with advanced-LIGO baseline mirror radii, and those for d'Ambrosio et. al.'s slightly larger mirrors ("fiducial" configurations). We present a brief conclusion in Sec. VII. For the readers interested in our numerical implementation of the eigenvalue problem, we include an Appendix where we sketch details of our computational work.

The results presented in this paper are based on previous work on nearly flat configurations by S. Vyatchanin [14] (some errors in this paper are corrected here) combined with recent analyses of nearly concentric cavities by P. Savov. An analytical proof of the duality relation between nearly flat and nearly confocal resonators by P. Savov and Y. Chen, and independently by E. D'Ambrosio and J. Agresti, will be provided in a companion paper [13].

2.2 Main formulas

The light inside LIGO arm cavities is well-described by the laws of diffraction optics in the paraxial approximation. The eigenvalue problem in this approximation for a half trip through a cavity with two identical axisymmetric mirrors can be written as

$$\int G(\vec{r}_1, \vec{r}_2)\, u(\vec{r}_2)\, d^2\vec{r}_2 = \lambda\, u(\vec{r}_1). \tag{2.1}$$

In the above equation $u(\vec{r})$ is an eigenmode of the cavity and λ is the corresponding eigenvalue. The eigenmode represents the state of the light (the electric field) on the surface of a mirror.

For advanced LIGO diffraction losses will be very small (about 10 ppm for each half trip), so it is an excellent idealization to ignore the losses and idealize the mirrors as infinite in radius. Then, $|\lambda| = 1$, G is a unitary operator, and its eigenvectors form a complete set. Each eigenmode u_{nm} and the corresponding eigenvalue λ_{nm} are labeled by two (*quantum*) numbers — radial (or principle) number $n = 0, 1, \ldots$ and angular (or azimuthal) number $m = 0, 1, \ldots$. All modes with angular number $m = 0$ are axisymmetric (no angular dependence), $m = 1$ are dipolar, $m = 2$ are quadrupole, etc.:

$$u_{nm} \propto e^{-im\varphi}. \tag{2.2}$$

The eigenmodes are normalized and orthogonal to each other according to the following definition:

$$\int u_{n_1 m_1}(\vec{r})\, u^*_{n_2 m_2}(\vec{r})\, d^2\vec{r} = \delta_{n_1 n_2}\, \delta_{m_1 m_2}\,. \tag{2.3}$$

We will use this set of eigenvectors as a basis for expanding the eigenmodes of cavities with tilted mirrors. The radial coordinate r is dimensionless and measured in units of the Fresnel diffraction size

$$b = \sqrt{L\lambda/2\pi}. \tag{2.4}$$

When the mirrors of a FP cavity are tilted in a symmetric way (as in Fig. 2.1b), the cavity's fundamental mode $u_{00}(\vec{r})$ is transformed into the fundamental mode $\tilde{u}_{00}(\vec{r})$ of the perturbed cavity. The torque acting on the mirrors when the light is in this mode and has power P is

$$T = \frac{2Pb}{c} \int \left|\tilde{u}_{00}(\vec{r})\right|^2 r \cos\varphi\, d^2\,\vec{r}. \tag{2.5}$$

The new fundamental mode can be expanded over the set of orthonormal modes $\{u_{nm}(\vec{r})\}$ of the unperturbed cavity

$$\tilde{u}_{00}(\vec{r}) = u_{00}(\vec{r}) + \sum_{n,m} \alpha_{nm} u_{nm}(\vec{r}). \tag{2.6}$$

In this paper, we study effects only to first order in the perturbation. That is why the coefficient in front of $u_{00}(\vec{r})$, in Eq. (2.6), is unity.

By substituting Eq. (2.6) into Eq. (2.5) and using the angular dependence of the eigenmodes Eq. (2.2), we conclude that only the dipolar eigenmodes ($m = 1$) contribute to the net torque and more specifically their part proportional to $\cos(\varphi)$. Thus, for our purposes of calculating the torque, we will assume $u_{n1} \propto \cos(\varphi)$. Since the only modes we use from now on are the fundamental mode u_{00} and all dipolar modes u_{n1}, in order to simplify notation, we collapse the indices into one labeling index

$$k = n + m. \tag{2.7}$$

Thus the fundamental mode becomes u_0, the first dipolar mode becomes u_1 (corresponding to the old notation u_{01}) and so on. When necessary, we will use the conventional notation with two labeling indices.

We will study the effects of tilt only to first order in the tilt angle θ, so for our purposes we use the following expansion of the perturbed eigenmode:

$$\begin{aligned}
\tilde{u}_0(\vec{r}) &= u_0(\vec{r}) + \sum_{k=1} \alpha_k u_k(\vec{r}), && (2.8)\\
u_0(\vec{r}) &= \frac{u_0(r)}{\sqrt{2\pi}}, && (2.9)\\
u_k(\vec{r}) &= \frac{u_k(r)\cos\varphi}{\sqrt{\pi}}, && (2.10)\\
\int_0^\infty \big[u_0(r)\big]^2 r\,dr &= 1, && (2.11)\\
\int_0^\infty \big[u_k(r)\big]^2 r\,dr &= 1, \qquad k = 1, 2, \ldots. && (2.12)
\end{aligned}$$

In the above equations, $u_k(\vec{r})$ are the dipolar modes on the surface of a mirror; $u_k(r)$ are their parts depending only on the radial coordinate r; all $u_k(r)$ are dimensionless and normalized as shown above [cf. Eq. (2.3) with $m = 0, 1, k = n + m$]; and α_k are dimensionless coupling constants, proportional to the mirrors' tilt angle θ, which we will evaluate in Sec. III for Gaussian (FG and CG) beams and in Sec. IV for mesa (FM and CM) beams. In general, $u_k(\vec{r})$ are complex fields, but since the mirror surfaces coincide with the beam's wave front, up to an overall complex phase which we chose to be zero, they are real fields.

Now we can calculate the torque that the cavity's light exerts on each mirror:

$$\begin{aligned} T &= \frac{2Pb}{c}\int \left[\tilde{u}_0(\vec{r})\right]^2 r\cos\varphi\, r\, dr\, d\varphi = \\ &= \frac{2Pb}{c}\, 2\sum_{k=1} \alpha_k \int u_0(\vec{r}) u_k(\vec{r})\, r\cos\varphi\, r\, dr\, d\varphi\,, \end{aligned}$$

where we have used Eq. (2.8). By inserting Eqs. (2.9) and (2.10), we obtain the following formulas for the tilt-induced torque to first order in α_k (first order in θ):

$$T = \frac{2\sqrt{2}\,Pb,}{c} \times \sum_{k=1} \alpha_k\, I_k, \tag{2.13}$$

$$I_k = \int u_0(r) u_k(r)\, r^2\, dr\,. \tag{2.14}$$

These formulas are valid for any FP cavity and in particular for FG, FM, CG, and CM cavities that interest us (of course, the modes $u_k(r)$ are different for different cavities).

In the sections below, we calculate the values for the coupling constants α_k and the overlap integrals I_k for our four types of cavities. Our analysis for conventional spherical mirrors (FG and CG; Sec. III) is entirely analytical, whereas for any generic mirror shape, and MH mirrors in particular (FM and CM; Sec IV), numerical treatment is required. We will test our numerical methods by applying them to FG and CG cavities and comparing with the analytical results.

2.3 Gaussian-Beam (FG and CG) Cavities

We consider a cavity with identical spherical mirrors. We are interested in a symmetric tilt of the two mirrors by a small angle θ as shown on Fig. 2.1b. In this case, the axis of the new mode $\tilde{u}_0(\vec{r})$ is displaced by a small distance $\delta x_{\rm sym}$, but is still parallel to the old axis. The field distribution on each mirror will be unchanged, but shifted by $\delta x_{\rm sym}$.

Spherical cavities have been studied thoroughly (see e.g [15]); their fundamental modes are the well-known Gauss-Laguerre modes (called in this paper FG and CG modes). We will use these modes derive analytical formulas for α_k and I_k. The main axisymmetric and dipolar modes [$u_0(r)$ and $u_1(r)$] are given by (see e.g. [16]):

$$\begin{aligned} u_0^G(r) &= \frac{\sqrt{2}}{r_0} e^{-r^2/2r_0^2}, && (2.15) \\ u_1^G(r) &= \frac{\sqrt{2}\,r}{r_0^2} e^{-r^2/2r_0^2}, && (2.16) \\ r_0 &= \frac{1}{(1-g^2)^{1/4}}. && (2.17) \end{aligned}$$

Here r is the dimensionless radial coordinate (measured in units of b), r_0 is the dimensionless radius of the beam at the mirrors' surface (also in units of b), $g = 1 - L/R$ is the so-called g-parameter of the cavity, L is the distance between the mirrors, and R is the mirrors' radius of curvature (Fig. 2.1a). (The intensity on the mirror is proportional to e^{-r^2/r_0^2}.)

For spherical mirrors the displacement of the optic axis δx_{sym} is (see Fig. 2.1b):

$$\delta x_{\text{sym}} \simeq \frac{R\theta}{b} = \frac{L\,\theta}{b(1-g)}. \qquad (2.18)$$

Next, we write down the main mode $\tilde{u}_0^G$ of the FP resonator with tilted mirrors and expand it to first order in δx_{sym}:

$$\begin{aligned} \tilde{u}_0^G(\vec{r}) &= \frac{e^{-r_{\delta x}^2/2r_0^2}}{\sqrt{\pi}}, && (2.19) \\ r_{\delta x}^2 &= \Big(r\cos\varphi - \delta x_{\text{sym}}\Big)^2 + r^2\sin^2\varphi, && (2.20) \\ \tilde{u}_0^G(\vec{r}) &= u_0^G(\vec{r})\left(1 + \frac{r\,\delta x_{\text{sym}}\,\cos\varphi}{r_0^2}\right) && \\ &= u_0^G(\vec{r}) + \frac{\delta x_{\text{sym}}\,\cos\varphi}{\sqrt{2\pi}r_0}\,u_1^G(r) && \\ &= u_0^G(\vec{r}) + \underbrace{\frac{\delta x_{\text{sym}}}{\sqrt{2}r_0}}_{\alpha_1^G}\underbrace{\frac{u_1^G(r)\,\cos\varphi}{\sqrt{\pi}}}_{u_1^G(\vec{r}).} && (2.21) \end{aligned}$$

As we can see, the only nonzero coupling constant is α_1^G

$$\alpha_1^G = \frac{L\,\theta\,(1+g)^{1/4}}{\sqrt{2}\,b\,(1-g)^{3/4}}. \qquad (2.22)$$

From Eqs. (2.14), (2.15), (2.16), and (2.17), we can easily calculate the only overlap integral we need for Gaussian beams:

$$\begin{aligned} I_1^G &= \int_0^\infty u_0^G(r) u_1^G(r)\, r^2\, dr = \\ &= r_0 = \frac{1}{(1-g^2)^{1/4}}. \end{aligned} \tag{2.23}$$

Substituting into Eq. (2.13) along with Eq. (2.22) we derive a final expression for the torque:

$$T^G = \frac{2PL}{c} \frac{\theta}{(1-g)}. \tag{2.24}$$

This result, derived by a modal analysis, is in complete agreement with the result of the Sidles-Sigg geometrical analysis in its *long-cavity* limit (Section 5 of [9]). In their notation, the torque for the unstable configuration is

$$T^G = -k_-\,\theta = \frac{2PL}{c} \frac{\theta}{(1-g)}, \tag{2.25}$$

where $-k_-$ is the negative eigenvalue of *a torsional stiffness matrix* (Eq. (23) of Section 5 in [9]). (Note that negative eigenvalues in the Sidles-Sigg analysis are associated with unstable configurations — the subject of interest in this paper.) Our perturbation method gives the exact result (to first order in θ) for spherical mirrors, because the only contribution to the torque is from the lowest dipolar mode u_1. This is a property only for spherical mirrors and their Gaussian beams. As we'll see in the following sections, for any generic mirror shapes, we have to calculate the contribution from all higher dipolar modes.

2.4 Mesa-Beam (FM and CM) Cavities: Analytical Formulas

Perfectly positioned mirrors (Fig. 2.1a). For any cavity with axisymmetric mirrors, and in particular MH mirrors, the main axisymmetric mode $u_0(\vec{r})$ and all dipolar modes $u_k(\vec{r})$ satisfy the integral eigenequations

$$\int G(\vec{r}_1, \vec{r}_2)\, u_0(\vec{r}_2)\, d^2\vec{r}_2 = \lambda_0\, u_0(\vec{r}_1), \tag{2.26}$$

$$\int G(\vec{r}_1, \vec{r}_2)\, u_k(\vec{r}_1)\, d^2\vec{r}_1 = \lambda_k\, u_k(\vec{r}_2), \tag{2.27}$$

where $G, u_0, u_k, \vec{r_1}, \vec{r_2}$ are all dimensionless and the eigenvalue of the k^{th} dipolar mode u_k is λ_k.

In the paraxial approximation, the kernel of the operator G is the following (up to a trivial factor of e^{ikL} due to phase accumulation along the arm length L, which we omit, thereby fixing a common overall phase factor in all the λ_k):

$$\begin{aligned} G(\vec{r_1}, \vec{r_2}) &= \frac{-i}{2\pi} \exp\left[i \left(\frac{(\vec{r_1} - \vec{r_2})^2}{2} - h_1(\vec{r_1}) - h_2(\vec{r_2}) \right) \right], \\ h_{1,2}(\vec{r}) &= k H_{1,2}(\vec{r}), \qquad k = \frac{2\pi}{\lambda}. \end{aligned} \tag{2.28}$$

Here $H_1(\vec{r_1})$ and $H_2(\vec{r_2})$ are the physical deviations of the mirrors' surfaces from a plane surface, which we assume to be the same, $H_1(\vec{r_1}) = H_2(\vec{r_2})$ (identical mirrors).

Symmetrically tilted mirrors (Fig. 2.1b). The tilt is equivalent to small deviations of each mirror's position from the unperturbed one:

$$\delta h_1 = kb\, r_1 \cos\varphi_1\ \theta \qquad \text{(left mirror)} \tag{2.29a}$$

$$\delta h_2 = kb\, r_2 \cos\varphi_2\ \theta \qquad \text{(right mirror).} \tag{2.29b}$$

These tilts induce a coupling of all the dipolar modes $u_1, u_2, \ldots$ into the cavity's fundamental mode $\tilde{u}_0$, as shown in Eq. (2.8), though (as our numerical work will show) the coupling for the first dipolar mode is far greater than the others $\alpha_1 I_1 \gg \alpha_k I_k$ for $k = 2, 3, \ldots$.

For simplicity, we will show the analysis only for the first dipolar mode u_1 (u_{01} in the conventional notation). The generalization for the higher dipolar modes is trivially obtained by replacing the subscript 1 by the desired dipolar mode's subscript k

The eigenvalue of the fundamental mode of the perturbed cavity $\tilde{\lambda}_0$ will slightly differ from λ_0: $\tilde{\lambda}_0 = \lambda_0 + \Delta$. Thus, we have the following integral eigenequation for $\tilde{u}_0(\vec{r})$

$$\begin{aligned} &(\lambda_0 + \Delta)[u_0(\vec{r_1}) + \alpha_1 u_1(\vec{r_1})] = \\ &= \int G(\vec{r_1}, \vec{r_2})[1 - i\,\delta h_1(\vec{r_1}) - i\delta h_2(\vec{r_2})] \\ &\qquad \times [u_0(\vec{r_2}) + \alpha_1 u_1(\vec{r_2})]\, d^2\vec{r_2}. \end{aligned} \tag{2.30}$$

This equation can be simplified by use of the eigenequation of the original unperturbed system (2.26):

$$\Delta u_0(\vec{r}_1) + (\lambda_0 + \Delta - \lambda_1)\alpha_1 u_1(\vec{r}_1) = \\ = -i\int G(\vec{r}_1, \vec{r}_2)[\,\delta h_1(\vec{r}_1) + \delta h_2(\vec{r}_2)]u_0(\vec{r}_2)\, d^2\vec{r}_2. \tag{2.31}$$

Here, we have dropped a term proportional to $\delta h\, \alpha_1 u_1$ in the integrand, since it is of second order in θ.

Multiplying Eq. (2.31) by $u_0(\vec{r}_1)$ and integrating over $d^2\vec{r}_1$, one can find that, to first order in θ, the correction Δ to the eigenvalue λ_0 is zero. Therefore, the correction of the eigenvalue has second order of smallness, so below we set $\Delta = 0$.

Multiplying Eq. (2.31) by $u_1(\vec{r}_1)$ and integrating over $d^2\vec{r}_1$, one can find α_1:

$$\begin{aligned}(\lambda_0 - \lambda_1)\alpha_1 &= -i(\lambda_0 + \lambda_1) \\ &\times \int u_0(\vec{r}_1)\, u_1(\vec{r}_1)\, \delta h_1(\vec{r}_1)\, d^2\vec{r}_1,\end{aligned}$$

so

$$\begin{aligned}\alpha_1 &= -\frac{ikb\,\theta\,(\lambda_0 + \lambda_1)}{\sqrt{2}(\lambda_0 - \lambda_1)} \underbrace{\int_0^\infty u_0(r)\, u_1(r)\, r^2\, dr}_{I_1} \\ &= -\frac{iL\, I_1 \theta(\lambda_0 + \lambda_1)}{\sqrt{2}b(\lambda_0 - \lambda_1)}.\end{aligned} \tag{2.32}$$

Similarly for the higher dipolar modes

$$\alpha_k = -\frac{iL\, I_k \theta(\lambda_0 + \lambda_k)}{\sqrt{2}b(\lambda_0 - \lambda_k)}. \tag{2.33}$$

In order to calculate the numerical value of α_k, we must solve the eigenequations (2.26) and (2.27) numerically for the eigenvalues λ_0, λ_k and the corresponding eigenfunctions $u_0(r)$, $u_k(r)$ (see Appendix 2.8 for details). The value of the integral I_k can be calculated numerically from Eq. (2.14).

Note that the formulas in this section are valid for any resonators with symmetric mirrors $H_1(r_1) = H_2(r_2)$ and very low diffraction losses, not just for mesa-beam resonators.

The coupling constant α_k is a measure of how much power is leaking out from the main resonant mode u_0 into a higher mode u_k. The torque exerted on the mirror is proportional to α_k [Eq. (2.13)] which depends on the relative location of the eigenvalues of the modes [Eq. (2.33)].

The best scenario would be if the cavity is designed so that $\lambda_0 = -\lambda_k$ for some dominant mode u_k so the contribution of this mode to the tilt instability is reduced to second order in the tilt angle θ. However, there wil still be a first-order contribution from the other modes that don't satisfy this property. As we shall see in Section VII, (luckily) the first dipolar mode of one of the configurations studied (nearly concentric mexican-hat mirrors) has this property $\lambda_0 = -\lambda_k$ almost satisfied and therefore this configuration is more stable compared than the others.

2.5 Numerical Solutions of Eigenequations

We have solved the eigenequations (2.26) and (2.27) numerically using the scheme described in Appendix 2.8, for our four cavity configurations: FG, CG, FM, and CM. Recall that our nearly flat and nearly concentric cavities were chosen such that the intensity $u_0(r)^2$ and therefore $u_0(r)$ at the mirrors' surfaces are identical (FG and CG are the same and FM and CM are the same). We have found numerically for FM and CM (mesa beams) and for FG and CG (Gaussian beams, Sec. III) that $u_k(r)$ is also the same for the nearly concentric and nearly flat cases. The eigenfunctions u_0 and u_1 are shown in Fig. 2.2. The eigenvalues, by contrast, are different for nearly flat and nearly concentric cavities, so we have four sets of eigenvalues (FG, CG, FM, CM), depicted in Fig. 2.3.

In our numerical solutions to the eigenequations (2.26) and (2.27), one of us (PS) found an interesting duality relation between nearly flat and nearly concentric configurations. This duality relation is satisfied for any generic mirror shape that satisfies the paraxial approximation. To within numerical error of less than 0.05 per cent, we found that a nearly concentric cavity, which has the same intensity profile as a nearly flat configuration, also has the same mirror-shape correction as the nearly flat cavity, but with opposite sign:[2]

$$\delta h^C(r) = -\delta h^F(r)\,. \tag{2.34}$$

Here $\delta h^C(r)$ is the deviation from concentric spherical shape, and $\delta h^F(r)$ is the deviation

---

[2] M.Bondarescu [12] was the first to discover this fact numerically, though for a specific set of light beams: his "hyperboloidal beams".

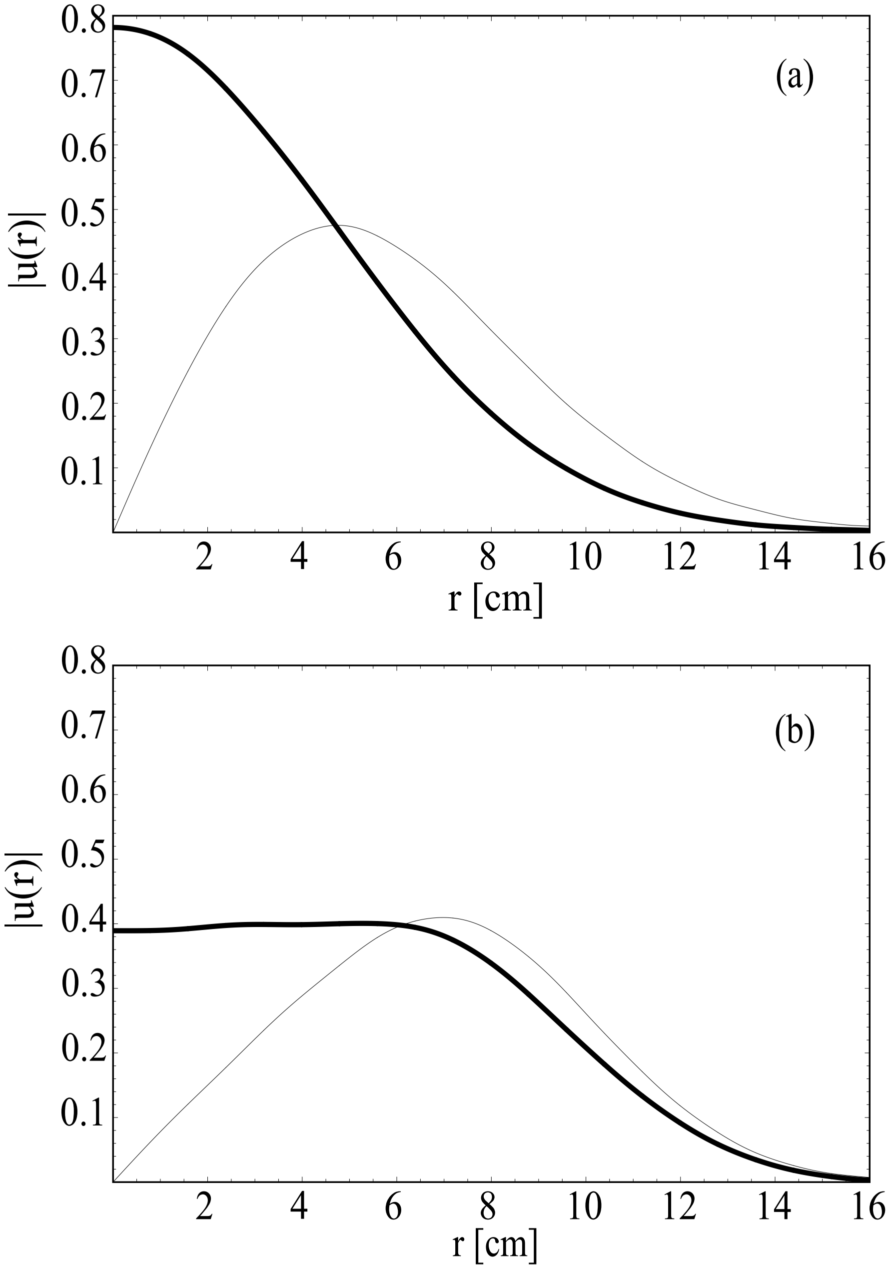

Figure 2.2: Fundamental modes $u_0(r)$ (thick curves) and first dipolar modes $u_1(r)$ (thin curves) at mirrors' surfaces for (a) FG and CG cavities, and (b) FM and CM cavities. The modes are dimensionless and normalized according to Eqs. (2.11), and(2.12). We have used the fiducial cavity parameters of d'Ambrosio et. al.: Eqs. (2) of Sec. IVA of [1] and Sec. IIIA of [2]

.

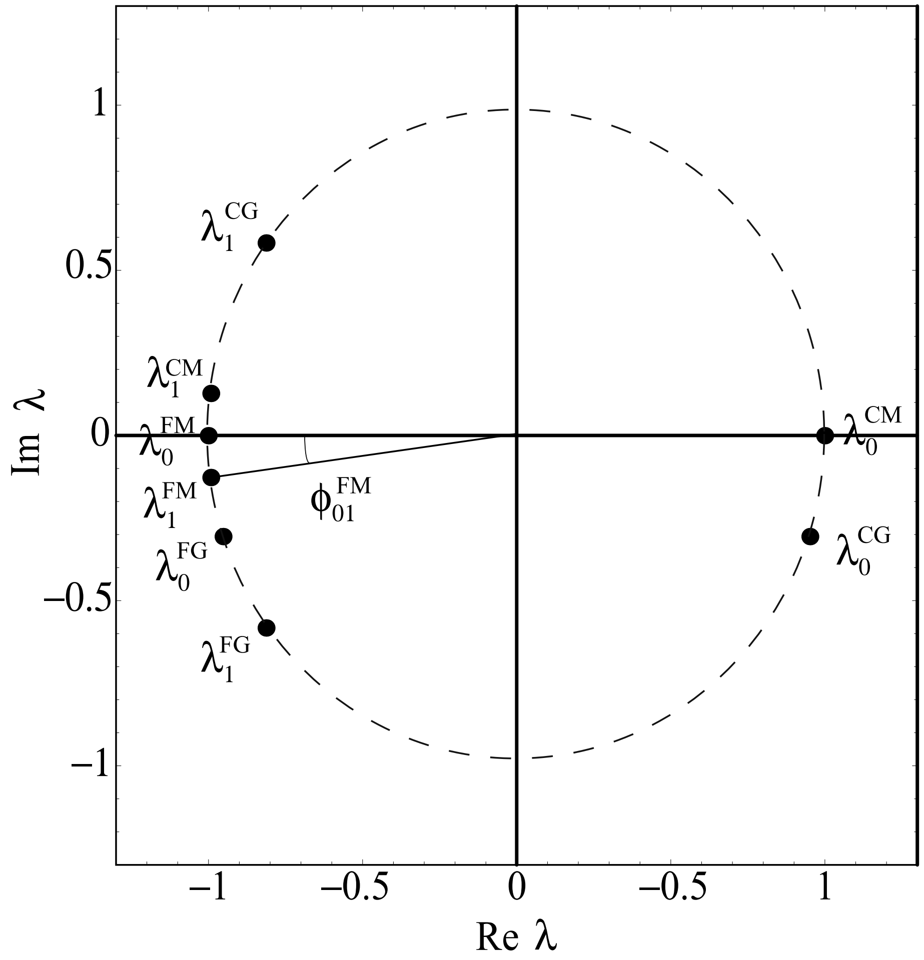

Figure 2.3: Eigenvalue spectrum in the complex plane. Note that all eigenvalues satisfy the duality relation, Eq. (2.35) ($n = 0,\ m = 0$ for λ_0, and $n = 0,\ m = 1$ for λ_1); see also [13].

from flat shape. We also found, numerically, a unique mapping between the eigenvalues of these dual configurations:

$$\lambda^C_{nm} = (-1)^{m+1}(\lambda^F_{nm})^*\,, \tag{2.35}$$

for any pair of integers $n, m = 0, 1, 2, \ldots$. In addition, all higher modes have the same intensity profiles at the mirrors' surfaces as their counterparts

$$|u^C_{nm}|^2 = |u^F_{nm}|^2 \tag{2.36}$$

for any integer $n, m = 0, 1, \ldots$.

Remarkably, our numerical calculations showed that these relations hold not just for mesa-beam cavities, but for all stable cavities that we explored (all mirror shapes $\delta h^{\mathrm{C,F}}$, including cavities in which the deviations $\delta h^{\mathrm{C,F}}$ from concentric spherical and flat shapes are large — as long as the paraxial approximation is valid).

This has led us to conjecture a *duality* relation between symmetric cavities with axisymmetric mirrors: for any two such cavities, A and B, with

$$h^{\mathrm{A}}(r) + h^{\mathrm{B}}(r) = \frac{r^2}{L} \tag{2.37}$$

there exists a one-to-one correspondence between their eigenstates: they all have the same intensity profiles at the mirrors, while

$$\lambda^{\mathrm{A}}_{nm} = (-1)^{m+1}(\lambda^{\mathrm{B}}_{nm})^*\,. \tag{2.38}$$

Chen and Savov, and independently Agresti and d'Ambrosio [13] have verified and generalized this conjecture analytically.

2.6 Strength of the Tilt Instability for FG, CG, FM, and CM cavities

We now have all the tools we need to compute the tilt-induced torque T on the cavity's mirrors, for FG, CG, FM, and CM configurations. We shall evaluate T for two sets of cavity parameters: the fiducial parameters used by d'Ambrosio et. al. [1, 2, 3] and the advanced-LIGO baseline parameters (Table 1 in [11]).

	Analytical		Numerical	
	FG	CG	FG	CG
I_1	1.8075	1.8075	1.8073	1.8073
α_1	0.012526	0.00030802	0.012525	0.00030799
T	0.064038	0.0015747	0.064023	0.0015743

Table 2.1: Comparison Between Analytical and Numerical Results for FG and CG Cavities; α_1 is measured in units of $(\theta/10^{-8})$ and T is in units of $(Pb/c)(\theta/10^{-8})$

The set of parameters for the fiducial cavity (see Sec. IV A(2) of [1] and Sec. III A of [2]) is:

$L = 4$ km — the length of the cavity.

$\lambda = 1064$ nm — the wavelength of the laser beam.

$k = 2\pi/\lambda$ — the wave number associated with λ.

$b = \sqrt{L\lambda/2\pi} = 2.603$ cm — the natural diffraction length scale (Fresnel length).

$r_{max} = 16$ cm — the radius of the mirrors' coated surfaces.

$g^{FG} = 0.952$ — the g-factor for the fiducial FG resonator (corresponding mirror radius of curvature $R = 83.33$ km).

$g^{CG} = -0.952$ — the g-factor for the fiducial CG resonator (corresponding mirror radius of curvature $R = 2.05$ km).

$r_0 = b/(1-g^2)^{1/4} = 4.7$ cm — the radius of the FG and CG beams at the mirrors.

$D = 4b = 10.4$ cm — the radius parameter of the FM and CM beams at the mirrors (see Sec. II A and Sec. IV A(2) of [1]).

The above beam radii were chosen so as to make the diffraction losses be about 20 parts per million (ppm). More specifically, they are 23 ppm for the FG and CG beams and 19 ppm for the FM and CM beams.[3]

From Eqs. (2.22), (2.23), and (2.13) we can calculate the integral I_1^G, the coupling constant α_1^G, and the torque T^G for the FG and CG cavities. Our results are shown in the second and third column of Table 2.1.

We have already established an agreement between our analytically derived results using the modal analysis described in Section III and the Sidles-Sigg results derived from geometric considerations [9]. We can also test the numerical first-order perturbation methods that we

---

[3] We have deduced these diffraction losses from our numerical solutions of the cavity's eigenequation.

developed for arbitrary mirror shapes by applying them to our FG and CG cavities. By substituting our numerical results for $u_0^{FG} = u_0^{CG}$, $u_1^{FG} = u_1^{CG}$, λ_0^{FG}, λ_0^{CG}, λ_1^{FG}, and λ_1^{CG} into Eqs. (2.23), (2.32), and (2.13), we calculate the results shown in the last two columns of Table 2.1. These numerical results all agree with our analytical results to within 0.05 per cent, thus validating our numerical methods.

As was found by Sidles and Sigg, the CG configuration is significantly less unstable than its nearly flat counterpart FG. The analytical analysis (first two columns in Table 2.1 predicts

$$\frac{T^{FG}}{T^{CG}} = \frac{1+g^{FG}}{1-g^{FG}} = \frac{R^{FG}}{R^{CG}} = 40.667, \tag{2.39}$$

which is in agreement with the numerical result 40.667 (last two columns).

From the modal analysis applied to FG and CG cavities [Eqs. (2.32) and (2.13)], we deduce that, aside from factors that are the same for FG and CG,

$$T^G \propto i\,\frac{\lambda_0^G + \lambda_1^G}{\lambda_0^G - \lambda_1^G} = \text{cotan}\left(\frac{\phi_{01}^G}{2}\right). \tag{2.40}$$

Here, the equality holds because $|\lambda| = 1$ for all modes (negligible diffraction losses) and ϕ_{01}^G is the phase separation between λ_0^G and λ_1^G, i.e. the argument of λ_0^G/λ_1^G (in Fig. 2.3 we show ϕ_{01}^{FM} for the FM cavity). Thus, Eq. (2.40) is governed by the phase separation of the eigenvalues λ_0^G and λ_1^G . As Fig. 2.3 shows the two eigenvalues for the FG configuration are very close to each other so $\text{cotan}(\phi_{01}^{FG}/2) \gg 1$, whereas the phase separation of the eigenvalues for the CG configuration is close to π so $\text{cotan}(\phi_{01}^{CG}/2) \ll 1$. This explains why $T^{FG} \gg T^{CG}$.

Similarly to the above Gaussian analysis, we use our numerical results to compute the torques T^{FM} and T^{CM} for FM and CM cavities respectively. In this case, we must include the contributions from higher order dipolar modes (u_1, u_2, and u_3). From Eqs. (2.13), (2.14), and (2.33), we have calculated the integrals I_k^{FM}, I_k^{CM}, the coupling constants $\alpha_k^{FM}, \alpha_k^{CM}$, and the torques T^{FM}, T^{CM} for the FM and CM cavities. Our results are shown in Table 2.2. Note that the dominant contribution to the torque comes from the first dipolar mode, $k = 1$; the higher modes give contributions of only a few per cent, at most.

For mesa-beam resonators, as in the case of Gaussian-beam resonators, the nearly flat

k	I_k^{FM}	α_k^{FM}	T_k^{FM}	I_k^{CM}	α_k^{CM}	T_k^{CM}
1	2.6464	0.04525	0.33867	2.6464	0.00018	0.00137
2	0.1136	0.00009	0.00003	0.1136	0.00016	0.00005
3	-0.015	-0.00000	0.00000	-0.015	-0.0002	0.00001
Total			0.33870			0.00143

Table 2.2: Numerical Results for FM and CM cavities; α_k is measured in units of $(\theta/10^{-8})$ and T_k is in units of $(Pb/c)(\theta/10^{-8})$

configuration (FM) is far more unstable than its nearly concentric counterpart (CM)

$$\frac{T^{FM}}{T^{CM}} = 237. \tag{2.41}$$

In this case, the difference is even bigger than in the Gaussian case since the eigenvalues for the FM configuration are closer to each other on the unit circle (Fig. 2.3) than for the FG configuration and the phase separation of the eigenvalues for the CM configuration is even closer to π than the phase separation of the eigenvalues for the CG configuration (Fig. 2.3).

In Table 2.3, we compare all four configurations FG, CG, FM, and CM, normalized by T^{CG}. For nearly flat resonators, going from a Gaussian-beam to a mesa-beam configuration increases the strength of the instability by about a factor 5. There are two effects contributing to this increase as we can see from the following relation (in which we focus on the dominant, $k = 1$ contribution):

$$\begin{aligned}\frac{T^M}{T^G} = \frac{\alpha_1^M I^M}{\alpha_1^M I^M} &= \left(\frac{\lambda_0^M + \lambda_1^M}{\lambda_0^G + \lambda_1^G}\right)\left(\frac{\lambda_0^G - \lambda_1^G}{\lambda_0^M - \lambda_1^M}\right)\left(\frac{I^M}{I^G}\right)^2 = \\ &= \frac{\text{cotan}\left(\phi_{01}^M/2\right)}{\text{cotan}\left(\phi_{01}^G/2\right)}\left(\frac{I^M}{I^G}\right)^2. \end{aligned} \tag{2.42}$$

In the case of the nearly flat configurations both phase differences are small and since $\phi_{01}^{FM} < \phi_{01}^{FG}$ (see Fig. 2.3),

$$\frac{\text{cotan}\left(\phi_{01}^{FM}/2\right)}{\text{cotan}\left(\phi_{01}^{FG}/2\right)} > 1.$$

This effect is amplified by the second ratio because of the higher overlap between the two eigenstates in the case of mesa beams than for Gaussian beams. This is manifested in the higher value of $I^{FM} = 2.65$ compared to $I^{FG} = 1.87$ (compare the overlaps between each

Table 2.3: Comparison between different configurations of a fiducial optical cavity. The torques due to light pressure (when tilt angle θ and circulating power P are the same) are normalized such that $T^{CG} = 1$.

	Nearly Flat Cavity	Nearly Concentric Cavity
G-Beam	$T^{FG} = 40.7$	$T^{CG} = 1.0$
M-Beam	$T^{FM} = 215$	$T^{CM} = 0.91$

pair of modes in Fig. 2.2a and Fig. 2.2b).

For nearly concentric resonators, going from Gaussian-beam resonators to mesa-beam resonators weakens the net instability: $T^{CM}/T^{CG} = 0.91$. In this case, the difference in the overlaps of the eigenstates is unchanged, but the phase differences are close to, but less than π. Since $\phi_{01}^{CM} > \phi_{01}^{CG}$ (again look at the separation of each set of eigenvalues on the unit circle for the CG and CM configurations in Fig. 2.3),

$$\frac{\operatorname{cotan}\left(\phi_{01}^{CM}/2\right)}{\operatorname{cotan}\left(\phi_{01}^{CG}/2\right)} < 1.$$

The two effects counteract each other and for this choice of parameters the net result is in favor of the CM-Beam resonator. The comparison between the torques for nearly flat and nearly concentric cavities is straightforward using Eq. (2.42) and the duality relation (see Eq. (2.35) and Ref. [13]).

In our formulation of the perturbation theory, we account for effects scaled to first order in the tilt angle θ. We assume small mode mixing $\alpha_k \ll 1$ in order for the perturbation method to work. From our numerical results (Table 2.2), we see that $\alpha_k \ll 1$ requires the angular orientation of the cavity mirrors be controlled to $\theta < 10^{-8}$.[4]

The contributions T_k of the higher order dipolar modes $k = 2, 3, \ldots$ to the torque can be understood by studying the analog of Eq. (2.42). From the relative locations of the eigenvalues along the unit circle and the overlapping of the eigenmodes, it is easy to show that T_k's are monotonically decreasing, $T_1 > T_2 > T_3 \ldots$. Thus, we accept the contribution from the highest dipolar mode u_3 in our calculation, including the numerical error, as the maximum error of the method due to neglecting the higher order dipolar modes. In this

---

[4] Currently, the control system of the initial LIGO interferometers operates with accuracy $\theta \simeq 10^{-7}$; an accuracy $\theta \simeq 10^{-8}$ is planned for advanced LIGO interferometers [17].

	Nearly Flat Cavity	Nearly Concentric Cavity
G-Beam	$T^{FG} = 26.2$	$T^{CG} = 1.0$
M-Beam	$T^{FM} = 96$	$T^{CM} = 0.91$

Table 2.4: Comparison between different configurations of a cavity with parameters of the current baseline design for advanced LIGO. The torques due to light pressure (when tilt angle θ and circulating power P are the same) are normalized such that $T^{CG} = 1$.

way, we conclude that the error in our total torque in the case of the CM cavity is less than 1 per cent. In the case of the FM cavity the error of the method is practically of order of the numerical error, so it is less than 0.1 per cent.

For another comparison, we perform the same calculations for the baseline design of advanced LIGO (Table 1 in [11]). The baseline parameters were chosen such that the beam radius at the mirrors[5] in the case of spherical mirrors is 4.24 cm, corresponding to diffraction losses of 10 ppm. The MH-mirror configurations are designed to have about the same diffraction losses. The resulting baseline parameters are:

$r_{max} = (15.7 - 0.8)$ cm $= 14.9$ cm — the radius of the coated mirrors' surfaces.

$g^{FG} = 0.9265$ — the g-factor for FG resonator (corresponding mirror radius of curvature $R = 54.44$ km).

$g^{CG} = -0.9265$ — the g-factor for CG resonator (corresponding mirror radius of curvature $R = 2.076$ km).

$r_0 = b/(1 - g^2)^{1/4} = 4.24$ cm — the radius of the Gaussian beam at the mirrors.

$D = 3.3b = 8.58$ cm — the radius parameter of the mesa beam at the mirrors.

Table 2.4 contains the final results for these baseline parameters (including the sum of the contributions to the torques from the first three dipolar modes). Again, the least unstable configuration, and thus the easiest to control against tilt, is the nearly concentric mesa-beam (CM) resonator.

2.7 Conclusions

In this paper, we have investigated the problem of the tilt instability for several possible configurations of advanced LIGO. By using semi-analytical and numerical techniques, we

---

[5] Note that our definition for the beam radius at the mirrors differs from [11] by factor of $\sqrt{2}$.

came to the conclusion that concentric Mexican-hat mirrors supporting mesa beams suffer the least instability and, therefore, pose the least problem to control the tilt instability. As Table 2.4 shows, by switching from conventional Gaussian-beam cavities to concentric mesa-beam cavities, the instability to symmetric tilt will be reduced (dramatically compared to a flat Gaussian-beam cavity and moderately compared to a concentric Gaussian-beam cavity). Furthermore the sensitivity of the interferometer will improve significantly due to the reduced thermal noise (see e.g. Table I in [3] and also [4, 5, 6, 18, 19]).

We have also reported on a unique duality relation between the eigenspectra of optical cavities with mirror shapes corrected from plane-parallel and from concentric spherical surfaces. The one-to-one mapping of the eigenvalues and the eigenmodes can be a very powerful tool in solving other problems involving modal analysis of optical cavities. In a companion paper [13], we provide an analytical proof and generalization of this conjecture.

2.8 Appendix A: Numerical Solutions of Cavity Eigenequations

In order to generate the set of basis solutions needed to construct perturbation theory for a cavity with arbitrary mirror shapes, we must numerically solve an integral eigenequation. We have done so using the following method, based on earlier work by O'Shaughnessy (Sec. V B of [3]).

Since the mirrors are axisymmetric [$h(\vec{r}) = h(r)$], we can decouple the angular and radial dependences in the eigenequations. In the numerical implementation of the eigensolver we used the following definition:

$$u_{nm}(\vec{r}) = u_{nm}(r)\, e^{-im\varphi}, \quad m = 0, 1, 2, \ldots . \tag{2.43}$$

Note that, for $m = 0, 1$, this definition of the fundamental radial mode $u_0(r)$ and the dipolar radial mode $u_1(r)$ differ from the definitions in Eqs. (2.9) and (2.10). However, after solving the eigenequations, all modes are renormalized by numerically computing the integrals in Eqs. (2.11) and (2.12), so at the end we have radial modes defined as in Eqs. (2.9) and (2.10). The resulting u_k are the radial modes we need for computing I_k in Eq. (2.14). By plugging Eq. (2.43) into Eqs. (2.26) and (2.27) and integrating over the azimuthal angle, we can reduce the eigenproblem to a one-dimensional integral equation

$$\begin{aligned} \lambda_{nm}\, u_{nm}(r_1) &= \int G_m(r_1, r_2)\, u_{nm}(r_2)\, r_2\, dr_2, \\ G_m(r_1, r_2) &= (-i)^{m+1} J_m(r_1 r_2) \\ &\times \exp\left[i \left(\frac{(r_1^2 + r_2^2)}{2} - 2h(r) \right) \right], \end{aligned} \tag{2.44}$$

where J_m is the Bessel function of the first kind and order m.

We discretize space along the mirrors' radial direction in a uniform grid

$$r_j = j\, r_{max}/(N-1), \quad j = 0, 1, \ldots, N-1. \tag{2.45}$$

We define the matrix $G_{(m)ij} = G_m(x_i, x_j)$, the eigenvectors $u_{(n)j} = u_n(x_j)$ (m, n label the mode and i, j are indices to access the matrices' and vectors' components), and we approximate the integration by a simple quadrature rule. Then the integral eigenproblem reduces to a matrix eigenvalue problem:

$$\lambda_{nm}\, \vec{u}_n = \hat{M}_m\, \vec{u}_n, \quad \text{with} \quad \hat{M}_{(m)ij} = \frac{r_{max}^2\, j}{N-1} G_{(m)ij}. \tag{2.46}$$

This equation can be solved for λ_{nm} and $\vec{u}_n$ by any standard matrix eigensolution software package.

Bibliography

[1] E. d'Ambrosio, R. O'Shaughnessy, S. Strigin, K.Thorne, and S. Vyatchanin, "Reducing Thermoelastic Noise in Gravitational-Wave Interferometers by Flattening the Light Beams", Phys. Rev. D, submitted; gr-qc/0409075

[2] E. D'Ambrosio, R. O'Shaughnessy, S. Strigin, K. Thorne, and S. Vyatchanin, "Status Report on Mexican-Hat Flat-Topped Beams for Advanced LIGO", LIGO-T030009-00; available at http://docuserv.ligo.caltech.edu/

[3] R. O'Shaughnessy, S. Strigin and, S. Vyatchanin, "The implications of Mexican-hat mirrors: calculations of thermoelastic noise and interferometer sensitivity to perturbation for Mexican-hat mirror proposal for advanced LIGO", Phys. Rev. D, submitted; gr-qc/0409050

[4] J. Agresti (2004), URL `http://www.ligo.caltech.edu/docs/T/T040225-00.pdf`.

[5] J. Agresi and R. DeSalvo (2005), URL `http://www.ligo.caltech.edu/docs/G/G050041-00/`.

[6] J. Agresti, paper in preparation.

[7] G. Lovelace, paper in preparation.

[8] D. Sigg, "Angular Instability in High Power FP Cavities" (2003), URL `http://www.ligo.caltech.edu/docs/T/T030120-00.pdf`.

[9] J. Sidles and D. Sigg, "Optical Torques in Suspended Fabry-Perot Interferometers", Phys. Lett. A **354**, 167 (2006).

[10] V. Braginsky and A. Manukin, *Measurement of weak forces in Physics Experiments*, (University of Chicago Press, 1977), pp. 25-39.

[11] D. Shoemaker, "Advanced LIGO: Context and Overview (Proposal to the NSF)" (2003), URL `http://www.ligo.caltech.edu/docs/M/M030023-00/`

[12] M. Bondarescu and K.S. Thorne, Phys. Rev. D, submitted; gr-qc/0409083

[13] J. Agresti, E. D'Ambrosio, Y. Chen, and P. Savov, Phys. Rev. D, submitted; gr-qc/0511062

[14] S. Vyatchanin, "Estimate of Angular Instability for Mexican-Hat and Gaussian Modes of a Fabry-Perot Interferometer" (2003), URL `http://www.ligo.caltech.edu/docs/T/T030272-00.pdf`.

[15] A. Siegman, *An Introduction to Lasers and Masers*, (McGraw-Hill, 1971), Ch. 8.

[16] A. Siegman, *Lasers*, (Univ. Science Book, 1996),Ch. 19.

[17] Daniel Sigg, private communication.

[18] V. Braginsky, M. Gorodetsky, and S. Vyatchanin, Phys. Lett. A **264**, 1 (1999).

[19] Y. T. Liu and K. Thorne, Phys. Rev. D **62**, 122002 (2000).

Chapter 3

Duality Relation Between Non-Spherical Optical Cavities

In his recent work on a tilt instability for advanced LIGO interferometers, P. Savov discovered numerically a unique duality relation between the eigenspectra of paraxial optical cavities with non-spherical mirrors: he found a one-to-one mapping between eigenstates and eigenvalues of cavities deviating from flat mirrors by $h(\vec{r}\,)$ and cavities deviating from concentric mirrors by $-h(\vec{r}\,)$, where h need not be a small perturbation. In this paper, we analytically prove and generalize this remarkable result. We then illustrate its application to interferometric gravitational-wave detectors; in particular, we employ it to confirm the numerical results of Savov and Vyatchanin for the impact of optical-pressure torques on LIGO's Fabry-Perot arm cavities (i.e. the tilt instability), when the mirrors are designed to support beams with rather flat intensity profiles over the mirror surfaces. This unique mapping might be very useful in future studies of alternative optical designs for LIGO interferometers, when an important feature is the intensity distribution on the cavity optics.

3.1 Introduction

Laser Interferometer Gravitational-wave Observatory (LIGO) [1] and other long baseline detectors, are formed by high-Finesse Fabry-Perot arms in order to increase the circulating optical power and to enhance sensitivities [2] by suppressing shot noise. LIGO interferometers, as well as the baseline design for *advanced-LIGO* detectors (whose funding is scheduled to begin in FY 2008) [3], all use spherical mirrors. Non-spherical mirrors have been alternatively studied and are considered for use in gravitational-wave interferometers, for the suppression of thermal noise they offer.

In particular, as shown by O'Shaughnessy, Thorne and Agresti [4, 5, 6, 7, 8], the thermal fluctuations of mirror surfaces are better averaged over by a flat beam, such a *mesa*-like [9] mode. The corresponding optical design has shown a strong tilt instability [10] and Thorne has proposed a different version of the *mesa beam*, that is supported by nearly *concentric* and opportunely shaped mirrors; this new version provides the same intensity profile at the cavity mirrors (and thus the same thermal noise), but imply a weaker tilt instability (even weaker than cavities with nearly concentric spherical mirrors analyzed by Sigg and Sidles [11, 12]) — as calculated by Savov and Vyatchanin [10] . A general method to design a family of optical cavities has been devised by Bondarescu and Thorne [13], from nearly flat resonators to nearly concentric ones.

Mesa beams are constructed by coherently overlapping Gaussian beams, with either(i) translated parallel axes, or (ii) axes in different directions but sharing a common midpoint [13]. Mirror shapes which support such beams as fundamental modes are derived from the phase fronts at the mirror locations, with case (i) corresponding to Mexican-hat mirrors, and case (ii) corresponding to the nearly-concentric version. Using the resulting optics profile, higher-order optical modes and eigenfrequencies of the designed cavities must be calculated by solving an eigenvalue problem, which has been done for nearly-flat cavities by O'Shaughnessy and Thorne [4, 3, 1, 2], and for nearly-concentric cavities by Savov and Vyatchanin [10]. During his numerical work, Savov discovered that the deviation of nearly-concentric Mexican-hat mirrors from concentric surfaces is exactly the opposite of the deviation of nearly-flat Mexican-hat mirrors from flat surfaces; he also found that the corresponding higher modes of these cavities all have the same intensity profiles, and that there is a one-to-one mapping between their eigenvalues. He went on and conjectured a general *duality relation* between axisymmetric cavities with two identical mirrors facing each other: cavities with mirrors deviating by $-h(|\vec{r}\,|)$ from concentric surfaces (*nearly concentric mirrors*) will support modes with the same intensity profiles and related eigenvalues as cavities with mirrors deviating by $h(|\vec{r}\,|)$ from flat surfaces (*nearly flat mirrors*). It should be noted that the deviation $h(\vec{r}\,)$ is *not* required to be infinitesimal, it can change the mirror shape arbitrarily *as long as the paraxial approximation is still satisfied*[1]. While such a duality relation is well-known between cavities with spherical mirrors, i.e., those with $h(\vec{r}) \sim \alpha \vec{r}^{\,2}$ (for example see [14, 15, 16, 17]), to our best knowledge no such relations had been established between generic cavities.

In this paper, we prove this remarkable correspondence analytically, for a even broader category of cavities: those whose mirror shapes remain invariant under the parity operation, identified as spatial reflection in the two dimensional $\vec{r}$-space (which is also equivalent to a 180° rotation around the cavity axis). Eigenmodes of such cavities can be put into eigenstates of parity, and we show that all corresponding eigenmodes of dual cavities have the same intensity profiles at the mirrors, with their eigenvalues satisfying

$$\gamma_{\mathrm{c}}^{k} = (-1)^{p_k+1} e^{-2ikL} (\gamma_{\mathrm{f}}^{k})^{*} \,, \tag{3.1}$$

where $(-1)^{p_k}$ is the parity of the kth eigenmode; subscripts c and f denote nearly concentric and nearly flat mirrors, respectively.

We will give two alternative proofs of this duality relation. The first one relies on the geometrical properties of the propagator from mirror to mirror. In this description the eigenfunctions are field amplitudes at mirror surfaces, and we see right away that the corresponding eigenstates have the same intensity profiles there. The second proof is based on the "center-to-center" propagator. The center-of-the-cavity fields are the eigenstates and the correspondence relation is manifested by a two-dimensional Fourier transform, that univocally relates the dual cavities.

This paper is organized as follows. In Sec. 3.2 we report the first proof; in Sec. 3.2.1, the Cartesian coordinates are used and some general features of the eigenproblem are described; in Sec. 3.2.2, the cylindrical coordinates are used, and the case of axisymmetric resonators is studied. Section 3.3 contains the second proof and the 2-D Fourier transform relation between the center-of-the-cavity eigenmodes of dual cavities. Section 3.4 specializes to the case of Mexican-hat cavities. When the nearly-flat and the nearly-concentric mirrors are implemented in the system, the corresponding mesa beams are connected by Fourier transform, as we report in Sec. 3.4.1. In Sec. 3.4.2, plots and analytical forms are provided,

---

[1] Here and henceforth in the paper a 2-D vector $\vec{r}$ has been used to indicate each point on planes orthogonal to the the cavity axis.

for the amplitude distributions at the center of the cavity and at the mirror surfaces; in Sec. 3.4.3, we address the tilt instability of the nearly concentric Mexican-hat resonator and show how easily it can be analyzed, applying the duality relation to the results obtained for the nearly flat Mexican-hat cavities [4, 3, 1]. We comment and review the implications of the general duality in Sec. 3.5.

3.2 Analytical proof for mirror-to-mirror propagation

3.2.1 In the Cartesian coordinate system

In this section we focus on field distributions on mirror surfaces, and restrict ourselves to cavities with two identical mirrors facing each other. The extension to the non non symmetric cavity is presented in Appendix A. We adopt the Fresnel-Kirchoff diffraction formula to propagate fields from mirror surface to mirror surface (see e.g. [16]). In this formalism, the field amplitude $v_1(\vec{r}\,')$ on the surface of mirror 1 propagates into

$$v_2(\vec{r}) = \int \mathrm{d}^2\vec{r}\,'\ \mathcal{K}(\vec{r},\vec{r}\,')\, v_1(\vec{r}\,') \tag{3.2}$$

on mirror 2, via the propagator

$$\mathcal{K}(\vec{r},\vec{r}\,') = \frac{ik}{4\pi\rho}(1+\cos\theta)e^{-ik\rho} \qquad\qquad k = \frac{2\pi}{\lambda}\,, \tag{3.3}$$

from $\vec{r}\,'$ (on mirror 1) to $\vec{r}$ (on mirror 2), where ρ denotes the (3-D) spatial distance between these two points and θ stands for the angle between the cavity axis and the reference straight line, as is illustrated in Fig. 3.1. We know that the Fresnel-Kirchoff integral eigenequation

$$\gamma\, v(\vec{r}) = \int \mathrm{d}^2\vec{r}\,'\ \mathcal{K}(\vec{r},\vec{r}\,')\, v(\vec{r}\,') \tag{3.4}$$

univocally determines the eigenmodes v and eigenvalues γ of the cavity.

Applying the paraxial approximation

$$\theta \approx 0\,, \quad \rho \approx L + \frac{|\vec{r}-\vec{r}\,'|^2}{2L} - h(\vec{r}) - h(\vec{r}\,')\,, \tag{3.5}$$

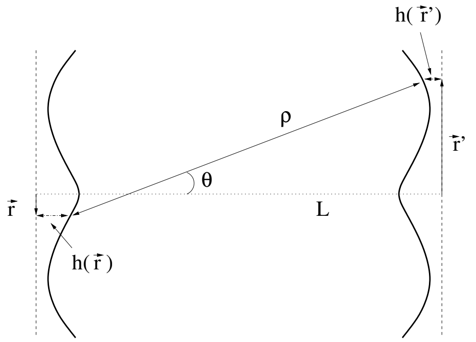

Figure 3.1: Symmetric Nearly Flat Mirrors.

and we can use

$$\mathcal{K}_{\mathrm{f}}^{h}(\vec{r},\vec{r}\,') = \frac{ik}{2\pi L}e^{-ikL}e^{ikh(\vec{r})}e^{-\frac{ik}{2L}|\vec{r}-\vec{r}\,'|^2}e^{ikh(\vec{r}\,')}\,. \tag{3.6}$$

in the integral eigenequation.

Here the mirror surfaces deviate by $h(\vec{r}\,)$ from a flat reference, and the subscript f is used to reflect this convention. From here on, we will also refer to $\mathcal{K}_{\mathrm{f}}^{h}$ as the *nearly flat propagator*. We now consider two slightly deformed concentric mirrors (see Fig. 3.2) so that the mirrors height with respect to the flat reference surface is

$$h(\vec{r}\,) = \vec{r}^{\,2}/L\, + b(\vec{r}\,)\,, \tag{3.7}$$

where the height $b(\vec{r}\,)$ is the deviation from the concentric spherical surface (note that concentric spherical mirrors have their radii of curvature equal to $L/2$, and thus surface height r^2/L). Inserting Eq. (3.7) into Eq. (3.5), we obtain the propagator for a *nearly-concentric* cavity,

$$\begin{aligned} \mathcal{K}_{\mathrm{c}}^{b}(\vec{r},\vec{r}\,') \quad &= \quad \frac{ik}{2\pi L}e^{-ikL} \\ &\qquad e^{ikb(\vec{r})}e^{+\frac{ik}{2L}|\vec{r}+\vec{r}\,'|^2}e^{ikb(\vec{r}\,')}\,. \end{aligned} \tag{3.8}$$

We use the term *nearly concentric* propagator for $\mathcal{K}_{\mathrm{c}}^{b}(\vec{r},\vec{r}\,')$. Although we use the terms *nearly-flat* and *nearly-concentric*, h and b are not required to be small; in fact, they can represent any deviation from perfectly flat and concentric spherical mirrors.

Now let us consider mirrors that are then invariant under parity, i.e., those in which we

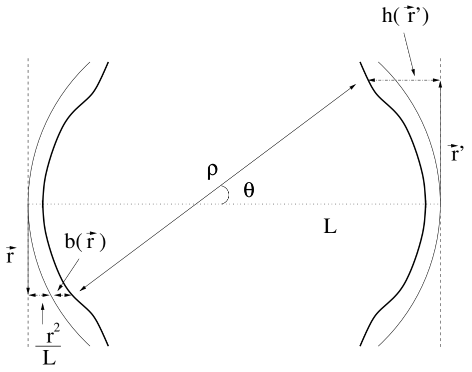

Figure 3.2: Symmetric Nearly Concentric Mirrors.

also have

$$h(\vec{r}) = h(-\vec{r})\,, \qquad b(\vec{r}) = b(-\vec{r})\,. \tag{3.9}$$

so that $\mathcal{K}_{\mathrm{f,\,c}}$ are both invariant under a spatial reflection

$$\left\{\vec{r}, \vec{r}\,'\right\} \leftrightarrow \left\{-\vec{r}, -\vec{r}\,'\right\} \tag{3.10}$$

and therefore, we have

$$\mathcal{P}\mathcal{K} = \mathcal{K}\mathcal{P}\,, \tag{3.11}$$

where we have defined

$$\mathcal{P}v(\vec{r}) = v(-\vec{r})\,. \tag{3.12}$$

for two dimensional reflection. Equation (3.11) implies that all eigenmodes can be put into forms with definite parity. We derive the following relation between nearly flat and nearly concentric propagators, as constructed:

$$\left[\mathcal{K}_{\mathrm{f}}^{h}(-\vec{r}, \vec{r}\,')\right]^{*} = -e^{2ikL}\mathcal{K}_{\mathrm{c}}^{-h}(\vec{r}, \vec{r}\,')\,, \tag{3.13}$$

that is equivalent to:

$$\mathcal{P}\left[\mathcal{K}_{\mathrm{f}}^{h}\right]^{*} = -e^{2ikL}\mathcal{K}_{\mathrm{c}}^{-h}\,. \tag{3.14}$$

Suppose we have an eigenstate v_{f} of $\mathcal{K}_{\mathrm{f}}^{h}$, i.e., an eigenstate of a cavity with mirror deviating by $(+h)$ from flat surface, and we compute its eigenvalue γ_{f} and know the parity eigenvalue

	Nearly Flat	Nearly Concentric
Kernel	$\mathcal{K}_{\mathrm{f}}^{h}$	$\mathcal{K}_{\mathrm{c}}^{-h}$
Eigenstate	v_{f}	v_{f}^{*}
Parity	$(-1)^{p}$	$(-1)^{p}$
Half-trip eigenvalue	γ_{f}	$e^{-2ikL}(-1)^{p+1}\gamma_{\mathrm{f}}^{*}$
Round-trip eigenvalue	η_{f}	$e^{-4ikL}\eta_{\mathrm{f}}^{*}$

Table 3.1: Correspondence of propagation kernels, eigenstates, parities, and eigenvalues between dual configurations.

$(-1)^p$:

$$\mathcal{K}_{\mathrm{f}}^{h} v_{\mathrm{f}} = \gamma_{\mathrm{f}}\, v_{\mathrm{f}}\,, \tag{3.15}$$

$$\mathcal{P} v_{\mathrm{f}} = (-1)^{p} v_{\mathrm{f}}\,. \tag{3.16}$$

By applying Eqs. (3.14)–(3.16), we derive the correspondence

$$\mathcal{K}_{\mathrm{c}}^{-h} v_{\mathrm{f}}^{*} = e^{-2ikL}(-1)^{p+1}\gamma_{\mathrm{f}}^{*} v_{\mathrm{f}}^{*}\,. \tag{3.17}$$

which identifies $v_{\mathrm{c}} \equiv v_{\mathrm{f}}^{*}$ as the corresponding eigenstate of $\mathcal{K}_{\mathrm{c}}^{-h}$, that is eigenstate of the corresponding resonator we denote the *dual*. The eigenvalue is $\gamma_{\mathrm{c}} \equiv e^{-2ikL}(-1)^{p+1}\gamma_{\mathrm{f}}^{*}$. We also induce that the parity is still $(-1)^{p}$. The reverse is straightforward and the result is an established one-to-one correspondence between dual cavities. We summarize this mapping in Table 3.1. It is obvious to note that that the corresponding eigenstates, v_{f} and v_{f}^{*}, have the same intensity profiles on the mirror surfaces; for infinite mirrors, we know $v_{\mathrm{f}}(\vec{r})$ is real-valued (see Appendix 3.7), so it is an eigenstate of the dual configuration itself.

For cavities with identical mirrors facing each other, the full, round-trip propagator is just the square of the half-trip one. From Eqs. (3.13) and (3.11), we have

$$\left[\left[\mathcal{K}_{\mathrm{f}}^{h}\right]^{2}\right]^{*} = e^{4ikL}\left[\mathcal{K}_{\mathrm{c}}^{-h}\right]^{2} \tag{3.18}$$

which means that the same duality correspondence exists between eigenstates of the full propagator, with their eigenvalues related by

$$\eta_{\mathrm{c}} = e^{-4ikL}\eta_{\mathrm{f}}^{*}\,. \tag{3.19}$$

Note that when $h(\vec{r}) = r^2/(2L)$ the two dual cavities are identical to each other. Using the relation that links the eigenvalues of two dual resonators, we can determine the spectrum

$$\gamma_c = \pm e^{-2ikL}\gamma_f^{*} = \gamma_f = e^{-ikL+in\pi/2}$$

where $n \in \mathcal{N}$. The resulting separation between the eigenvalues is the Gouy phase

$$e^{i\theta_G} = e^{i\arccos(1-L/R)} \qquad R = L$$

computed for confocal resonators [15, 16, 17].

3.2.2 Specializing to cylindrical mirrors

In most LIGO applications, cavity mirrors still have cylindrical shapes: $h(\vec{r}\,) = h(|\vec{r}\,|)$. This allows us to decouple radial and azimuthal degrees of freedom, and simplify the eigenvalue problem. We shall follow roughly the notation of [17].

We adopt the cylindrical coordinate system:

$$\vec{r} = r(\cos\varphi, \sin\varphi)\,. \tag{3.20}$$

Since $\mathcal{K}$ is now invariant under rotation along the z-axis, all eigenmodes can be put into eigenstates of rotation:

$$v(r,\varphi) = R(r)e^{-im\varphi}\,, \quad m = \text{integer}\,. \tag{3.21}$$

Inserting this into the eigenequation (3.4) and performing analytically the angular integration we obtain the radial eigenequation

$$\gamma_{nm}R_{nm}(r) = \int_0^a K^{h}_{\mathrm{f}(m)}(r,r')R_{nm}(r')r'dr'\,, \tag{3.22}$$

where for each angular mode number m we have indexed the radial eigenstates by n, and

$$K^h_{\mathrm{f}(m)}(r,r') = \frac{i^{m+1}k}{L} J_m\left(\frac{krr'}{L}\right) e^{ik\left[-L+h(r)+h(r')-\frac{r^2+r'^2}{2L}\right]} \tag{3.23}$$

is a symmetric radial propagator, in the *nearly-flat* description.[2] Since $K^h_{\mathrm{f}(m)}(r,r')$ is symmetric, we obtain orthogonality relations between radial eigenfunctions:

$$\int_0^a R_{n_1m}(r)R_{n_2m}(r)rdr = \delta_{n_1n_2}\,. \tag{3.24}$$

Using Eq. (3.7) again, for a configuration with $b(r)$ correction from concentric spherical mirrors, we obtain the radial kernel of the *nearly-concentric* description:

$$K^b_{\mathrm{c}(m)}(r,r') = \frac{i^{m+1}k}{L} J_m\left(\frac{krr'}{L}\right) e^{ik\left[-L+b(r)+b(r')+\frac{r^2+r'^2}{2L}\right]}\,. \tag{3.25}$$

Comparing Eqs. (3.25) and (3.23), we obtain:

$$(-1)^{m+1}\left[K^h_{\mathrm{f}(m)}\right]^* = e^{2ikL}K^{-h}_{\mathrm{c}(m)}\,. \tag{3.26}$$

This is a radial version of Eq. (3.14); here we know explicitly that all m-eigenstates have parity $(-1)^m$.

Following a similar reasoning as done in the previous section, *for each* angular mode number m, we can establish a one-to-one correspondence between radial eigenstates of a nearly-flat configuration to those of the dual configuration:

$$[R_{nm}]_{\mathrm{c}} = [R_{nm}]^*_{\mathrm{f}}\,. \tag{3.27}$$

The mapping of the eigenvalues are given by

$$[\gamma_{nm}]_{\mathrm{c}} = (-1)^{m+1}e^{-2ikL}\,[\gamma_{nm}]^*_{\mathrm{f}}\,. \tag{3.28}$$

Similarly, the round-trip eigenstates have the same correspondence, their eigenvalues related

---

[2] Here we have used $J_n(z) = \dfrac{1}{2\pi i^n}\displaystyle\int_0^{2\pi} e^{iz\cos\varphi}e^{in\varphi}d\varphi$, where $J_n(z)$ is the nth order Bessel function of the first kind.

by

$$[\eta_{nm}]_{\mathrm{c}} = e^{-4ikL}\,[\eta_{nm}]_{\mathrm{f}}^{*}\,. \tag{3.29}$$

3.3 Analytical proof based on center-to-center propagation

3.3.1 Propagators for vacuum and mirror surfaces

In this section, we focus on complex amplitudes of the optical field on planes perpendicular to the optical axis (the z axis). An optical mode propagating along one direction of the optical axis can be specified completely by the distribution of the field on the $z = \mathrm{const}$ plane. For example, we denote the optical field on the plane $z = z_1$ by $v(\vec{r}, z_1)$, where $\vec{r}$ is the 2-D coordinate of the point on this plane. The effect of any linear paraxial optical system (including open space, thin lenses and mirrors) with input plane z_1 and output plane z_2 can be characterized by its *transfer operator*, $\mathcal{U}$, which takes the form of an integration kernel:

$$v(\vec{r}, z_2) = \int d^2\vec{r}\,'\,\mathcal{U}(\vec{r}, z_2; \vec{r}\,', z_1)v(\vec{r}\,', z_1)\,. \tag{3.30}$$

In particular, the operator that describes the paraxial propagation down a length L in vacuum is

$$\mathcal{G}_L(\vec{r}, \vec{r}\,') = i\frac{k}{2\pi L}e^{-ikL}\exp\left[-ik\frac{(\vec{r}-\vec{r}\,')^2}{2L}\right]\,. \tag{3.31}$$

For a mode propagating in the $\pm z$ direction with field (complex) amplitude distribution $v(\vec{r}\,', z_1)$ at $z = z_1$, the amplitude distribution on a surface described by height $z(\vec{r}) = z_1 \mp h(\vec{r})$ is given by

$$v[\vec{r}, z(\vec{r})] = e^{\pm ikh(\vec{r})}v[\vec{r}, z_1]\,. \tag{3.32}$$

Here we emphasize that the spatial point of interest is located outside the $z = z_1$ plane, and that the 2-D vector $\vec{r}$ describes the projection of that point onto the $z = z_1$ plane.

From Eq. (3.32), one deduces that the operator for reflection off a perfect infinite mirror with shape $h(\vec{r})$ is[3]

$$\mathcal{R}_{[h(\vec{r})]}(\vec{r}, \vec{r}\,') \equiv -\delta(\vec{r}-\vec{r}\,')e^{2ikh(\vec{r})}. \tag{3.33}$$

It is easy to verify that both $\mathcal{G}_L$ and $\mathcal{R}_{[h(\vec{r})]}$ are unitary operators.

---

[3] The minus sign in Eq. (3.33) is used because we use a convention in which a phase shift by π is gained upon reflection.

3.3.2 Analytical proof based on center-to-center propagation

In this section we present an alternative proof motivated from the construction of the flat-topped beams [3, 10]: (i) the nearly flat configuration has its fundamental mode generated by *spatial translation* of minimal Gaussian beams, while (ii) the nearly concentric configuration is generated by *rotation* (of propagation direction at the center of cavity) of minimal Gaussian beams, or a translation in the momentum $\vec{k}$-space. This had led us to speculate that the two sets of eigenstates correspond to each other via *Fourier transform* (similar to the relation between position and momentum space in quantum mechanics).

We will use the operator $\mathcal{G}_{L/2}$ [see Eq. (3.31)] which propagates the field forward by *half* the cavity length. For simplicity we denote it by $\mathcal{G}$:

$$\mathcal{G}(\vec{r},\vec{r}\,') \equiv i\frac{k}{\pi L}e^{-ikL/2}e^{-ik\frac{(\vec{r}-\vec{r}\,')^2}{L}} . \tag{3.34}$$

Using $\mathcal{G}$ and $\mathcal{R}_{h(\vec{r})}$ [defined in Eq. (3.33), with $h(\vec{r})$ the mirror surface height], we can re-express the eigenvalue problem as:

$$\mathcal{L}_{[h(\vec{r})]}u \equiv \mathcal{G}\mathcal{R}_{[h(\vec{r})]}\mathcal{G}u = \gamma u , \tag{3.35}$$

with $\mathcal{L}_{[h(\vec{r})]}$ the center-to-center propagator when the mirror deviates from flat surfaces by $h(\vec{r})$, in which the optical mode propagates from the cavity center to the mirror, gets reflected, and propagates back to the center. In fact, $\mathcal{L}$ is related to the surface-to-surface propagator $\mathcal{K}$ by a unitary transformation,

$$\mathcal{L} = \mathcal{G}^{-1}\mathcal{R}^{-1}_{[h(\vec{r})/2]}\mathcal{K}\mathcal{R}_{[h(\vec{r})/2]}\mathcal{G} . \tag{3.36}$$

This means the two proofs are mathematically equivalent. Similar to $\mathcal{K}$, the operator $\mathcal{L}$ also commutes with parity, or [Cf. Eq. (3.11)]

$$\mathcal{P}\mathcal{L} = \mathcal{L}\mathcal{P} ; \tag{3.37}$$

With the propagator on hand, we proceed with our intuition that the modes must be related by Fourier transforms. In order to do so, we first define the 2-D Fourier-transform operator $\mathcal{F}$ as

$$\mathcal{F}(\vec{r},\vec{r}') = \frac{k}{\pi L} e^{-\frac{2ik}{L}\vec{r}\cdot\vec{r}'}\,, \tag{3.38}$$

which satisfies

$$\mathcal{F}^2 = (\mathcal{F}^{-1})^2 = \mathcal{P}\,. \tag{3.39}$$

It is easy to show that,

$$\begin{aligned} & \left[\mathcal{G}^*\mathcal{F}^{-1}\right](\vec{r},\vec{r}\,') \\ = & -\frac{ik^2}{\pi^2 L^2} e^{ik\left[\frac{L}{2}+\frac{\vec{r}^2}{L}+\frac{(\vec{r}-\vec{r}')^2}{L}\right]} \int d^2\vec{r}\,'' e^{\frac{ik}{L}[\vec{r}\,''-(\vec{r}-\vec{r}\,')]^2} \\ = & \left[ie^{ikL}\mathcal{R}_{[\vec{r}^2/(2L)]}\mathcal{G}\right](\vec{r},\vec{r}\,')\,. \end{aligned} \tag{3.40}$$

[The integral on the second line can be done by inserting a factor $e^{-\epsilon(\vec{r}\,'')^2}$ into the integrand, and then letting $\epsilon \to 0^+$.] Similarly, [or by taking the transpose of Eq. (3.40)], we have

$$\mathcal{F}^{-1}\mathcal{G}^* ie^{ikL}\mathcal{G}\mathcal{R}_{[\vec{r}^2/(2L)]}\,. \tag{3.41}$$

Using Eqs. (3.40) and (3.41), we have

$$\begin{aligned} & \mathcal{P}\mathcal{L}^*_{[h_{\mathrm{A}}]} \\ = & \mathcal{F}^{-1}(\mathcal{F}^{-1}\mathcal{G}^*)\mathcal{R}_{[-h_{\mathrm{A}}]}(\mathcal{G}^*\mathcal{F}^{-1})\mathcal{F} \\ = & -e^{2ikL}\mathcal{F}^{-1}\mathcal{G}\mathcal{R}_{[\vec{r}^2/(2L)]}\mathcal{R}_{[-h_{\mathrm{A}}]}\mathcal{R}_{[\vec{r}^2/(2L)]}\mathcal{G}\mathcal{F} \\ = & -e^{2ikL}\mathcal{F}^{-1}\mathcal{L}_{[h_{\mathrm{B}}]}\mathcal{F}\,. \end{aligned} \tag{3.42}$$

Here h_{A} and h_{B} are mirror heights related by the duality relation,

$$h_A(\vec{r}) + h_B(\vec{r}) = r^2/L\,, \tag{3.43}$$

and we have used the fact that

$$\mathcal{R}_{[\vec{r}^2/(2L)]}\mathcal{R}_{[-h_{\mathrm{A}}]}\mathcal{R}_{[\vec{r}^2/(2L)]} = \mathcal{R}_{[\vec{r}^2/L-h_{\mathrm{A}}]} = \mathcal{R}_{[h_{\mathrm{B}}]}\,. \tag{3.44}$$

According to Eq. (3.42), given any eigenstate u_A of $\mathcal{L}_{[h_{\mathrm{A}}]}$ with eigenvalue γ_{A} and a definite parity of p, we have

$$\begin{aligned} (-1)^p \gamma_{\mathrm{A}}^* u_A^* &= \mathcal{P}\mathcal{L}_{[h_{\mathrm{A}}]}^* u_A^* \\ &= -e^{2ikL}\mathcal{F}^{-1}\mathcal{L}_{[h_{\mathrm{B}}]}(\mathcal{F}u_A^*)\,, \qquad (3.45) \\ \Rightarrow \mathcal{L}_{[h_{\mathrm{B}}]}(\mathcal{F}u_A^*) &= (-1)^{p+1}e^{-2ikL}\gamma_{\mathrm{A}}^*(\mathcal{F}u_A^*)\,. \qquad (3.46) \end{aligned}$$

In other words, the mapping

$$u_{\mathrm{A}} \quad\rightarrow\quad u_{\mathrm{B}} = \mathcal{F}u_A^* \tag{3.47}$$

transforms each eigenstate of $\mathcal{L}_{[h_{\mathrm{A}}]}$ into its dual one of $\mathcal{L}_{[h_{\mathrm{B}}]}$; the corresponding eigenvalue relation is

$$\gamma_{\mathrm{B}} = (-1)^{p+1}e^{-2ikL}\gamma_{\mathrm{A}}^*\,. \tag{3.48}$$

For similar reasons, given any eigenstate u_{B} of $U_{[h_{\mathrm{B}}]}$ (with definite parity), $\mathcal{F}u_{\mathrm{B}}^*$ must also be an eigenstate of $U_{[h_{\mathrm{A}}]}$. Moreover, since

$$\mathcal{F}(\mathcal{F}u_{\mathrm{B}}^*)^* = \mathcal{F}\mathcal{F}^{-1}u_{\mathrm{B}} = u_{\mathrm{B}}\,, \tag{3.49}$$

the state $\mathcal{F}u_{\mathrm{B}}^*$ is in fact the inverse image of u_{B} [under the mapping (3.47)]. This means we have established a one-to-one correspondence between eigenstates of $\mathcal{L}_{[h_{\mathrm{A}}]}$ and those of $\mathcal{L}_{[h_{\mathrm{B}}]}$.

Now let us look at intensity profiles on the end mirrors surface. For the eigenstate u_{A}, the field amplitude at the constant-z plane of the end mirror is $\mathcal{G}u_{\mathrm{A}}$. For its image eigenstate $u_B \equiv \mathcal{F}u_{\mathrm{A}}^*$, we have

$$\begin{aligned} \mathcal{G}u_{\mathrm{B}} = \mathcal{G}(\mathcal{F}u_{\mathrm{A}}^*) &= \left[\mathcal{G}^*\mathcal{F}^{-1}u_{\mathrm{A}}\right]^* \\ &= \left[ie^{ikL}R_{[\vec{r}^2/(2L)]}\mathcal{G}u_{\mathrm{A}}\right]^* \qquad (3.50) \end{aligned}$$

which does have the same intensity profile [see Eq. (3.33)].

For the round-trip propagator $\mathcal{L}^2$, using Eqs. (3.42) and (3.37), we have

$$\left[\mathcal{L}_{[h_{\mathrm{A}}]}^2\right]^* = e^{4ikL}\mathcal{F}^{-1}\mathcal{L}_{[h_{\mathrm{B}}]}^2\mathcal{F}\,, \tag{3.51}$$

so we have the same duality correspondence (3.47) between eigenstates of the full propagator, with the mapping between eigenvalues given by

$$\eta_{\mathrm{B}} = e^{-4ikL}\eta_{\mathrm{A}}^{*}\,. \tag{3.52}$$

3.4 Application of the duality relation using Mesa Beams and Mexican-Hat cavities

The mesa beams were constructed to have flat-topped intensity profiles at the cavity mirrors with rapid fall-off near mirror rims, in order to achieve lower thermal noises [4, 3, 1, 2]. There are two versions of mesa beams with the same intensity profile, the nearly flat and the nearly concentric. Cavities that support them (Mexican-Hat cavities) are related by the duality relation, as realized by Savov [10], during his study of radiation-pressure-induced tilt instabilities. In this section, we shall explicitly construct these two fundamental modes, study their relations at the center of the cavity, and at the cavity mirrors. We will also discuss analytical features of the two modes that have not been obtained before. We will also give an example of how the calculation of the tilt instability can be dramatically simplified for nearly concentric Mexican-hat cavities, using the duality relation, based on results already obtained for the nearly flat configuration.

3.4.1 Construction of Mesa beams in Cartesian coordinate system

Nearly-flat Mesa beams are constructed by coherently superimposing minimal Gaussians, namely Gaussian modes with the smallest possible spot size at the cavity mirrors, $\sigma_{\mathrm{min}} = \sqrt{L/(2k)}$, whose axes are parallel to the cavity axis and lie within a cylinder centered at the cavity axis. At the middle of the cavity, the axes intercept with the constant-z plane in a disk $\mathcal{D}$, with radius p. It is evident that such a construction will give a rather flat intensity profile in the central region of the end mirror with radius $\sim p$; beyond this radius, the intensity profile falls off as a Gaussian with decay length σ_{min}, which is conceivably the fastest possible [3, 1, 2].

The complex amplitude of the nearly-flat mesa beam (fundamental mode of the corresponding cavity) at the center of the cavity is of the form

$$v_{\rm f}(\vec{r}\,) = \int_{\vec{r}_0 \in \mathcal{D}} d^2\vec{r}_0 \left(\frac{1}{\sqrt{2\pi}\sigma}\right)^2 e^{-\frac{(\vec{r}-\vec{r}_0)^2}{2\sigma^2}}\,, \tag{3.53}$$

Here σ is the waist size, which we leave general (rather than setting $\sigma = \sigma_{\rm min}$) for the moment. The duality image of $v_{\rm f}$ is

$$\begin{aligned} v_{\rm c}(\vec{r}\,) &= [\mathcal{F}v_{\rm f}^*](\vec{r}\,) \\ &= \int_{\vec{r}_0 \in \mathcal{D}} d^2\vec{r}_0\, e^{\frac{2ik\vec{r}\cdot\vec{r}_0}{L}} \mathcal{F}\left[\left(\frac{1}{\sqrt{2\pi}\sigma}\right)^2 e^{-\frac{\vec{r}^{\,2}}{2\sigma^2}}\right] \\ &= \int_{\vec{r}_0 \in \mathcal{D}} d^2\vec{r}_0\, e^{\frac{2ik\vec{r}\cdot\vec{r}_0}{L}} \left[\left(\frac{1}{\sqrt{2\pi}\sigma_*}\right)^2 e^{-\frac{\vec{r}^{\,2}}{2\sigma_*^2}}\right], \end{aligned} \tag{3.54}$$

with

$$\sigma\sigma_* = \frac{L}{2k} = \sigma_{\rm min}^2\,, \tag{3.55}$$

When going from Eq. (3.53) to Eq. (3.54), the Fourier transform has been completed by two steps. First, the spatial translation by $\vec{r}_0$ is replaced by the phase factor of $e^{\frac{2ik\vec{r}\cdot\vec{r}_0}{L}}$, which represents a tilt of the propagation axis by an angle of $2\vec{r}_0/L$. Second, the σ-Gaussians turn into σ_*-Gaussians. [This correspondence between Gaussians in fact reflects the duality between pairs of spherical cavities.] As a consequence, $v_{\rm c}$ represents the superposition of Gaussians with symmetry axes going through the cavity center, but with tilt angles distributed uniformly in a disk with radius $2p/L$ — exactly the construction of a nearly-concentric mesa beam. In particular, Eq. (3.55) tells us that minimal Gaussian would have turned into itself in this process. Hence we have shown explicitly the correspondence between the nearly-flat and nearly-concentric mesa beams (the fundamental modes of the corresponding cavities).

3.4.2 Profiles of mesa beams and mirror shapes

In order to study mesa beams in more details, we adopt the cylindrical polar coordinate system (r, ϕ); the cylindrical symmetry of these beams will make the complex amplitude only depend on r. Equations (3.53) and (3.54), written in the polar coordinate system, become

$$\begin{aligned} v_{\rm f}^{\rm waist}(r,\phi) &= \frac{1}{\pi w_0^2}\int_0^p r_0 {\rm d}r_0 \\ &\quad \int_0^{2\pi} {\rm d}\phi_0\, e^{-\frac{r^2-2r_0 r\cos(\phi-\phi_0)+r_0^2}{w_0^2}}\,, \qquad (3.56)\\ v_c^{\rm waist}(r,\phi) &= \frac{1}{\pi w_0^2}\int_0^p r_0 {\rm d}r_0 \\ &\quad \int_0^{2\pi} {\rm d}\phi_0\, e^{-\frac{r^2+2ir_0 r\cos(\phi-\phi_0)}{w_0^2}}\,. \qquad (3.57)\end{aligned}$$

Here $w_0 = \sqrt{L/k} = \sqrt{2}\sigma_{\rm min}$ and L is the total length of the cavity. Carrying out the angular integrations analytically, we get

$$v_{\rm f}^{\rm waist}(r) = \int_0^{p/w_0} 2x_0 e^{-(x^2+x_0^2)} I_0(2xx_0)dx_0\,, \qquad (3.58)$$

$$v_{\rm c}^{\rm waist}(r) = \frac{1}{x}e^{-x^2}J_1(2xp/w_0)\,, \qquad (3.59)$$

where $x \equiv r/w_0$, and I_0 is the modified Bessel function of the first kind. Examples of normalized power distributions of nearly flat and nearly concentric mesa beams are plotted in the upper panels of Fig. 3.3. In these plots, we take $p = 4w_0$, which corresponds to the configuration proposed for Advanced LIGO (for reasons that will be explained in Sec. 3.4.3).

Let us analyze these amplitude distributions in more details, in the case of $p \gg w_0$, i.e., when we translate the minimal Gaussians by a distance substantially greater than their waist size. For the nearly-flat configuration, we can easily see from Eq. (3.53) that, when $(p-r)/w_0 \gg 1$, the field distribution can be approximated as

$$v_{\rm f}(r \ll p) \approx \int_{\vec r_0 \in \mathbf{R}^2} d^2\vec r_0 \left(\frac{1}{\sqrt{2\pi}\sigma}\right)^2 e^{-\frac{(\vec r-\vec r_0)^2}{2\sigma^2}} = 1\,. \qquad (3.60)$$

On the other hand, if r is much larger than w_0 [since $p \gg w_0$, this region overlaps with the previous one], we can apply the asymptotic expansion of I_0

$$I_0(z) = \frac{1}{\sqrt{2\pi z}}e^z \qquad (3.61)$$

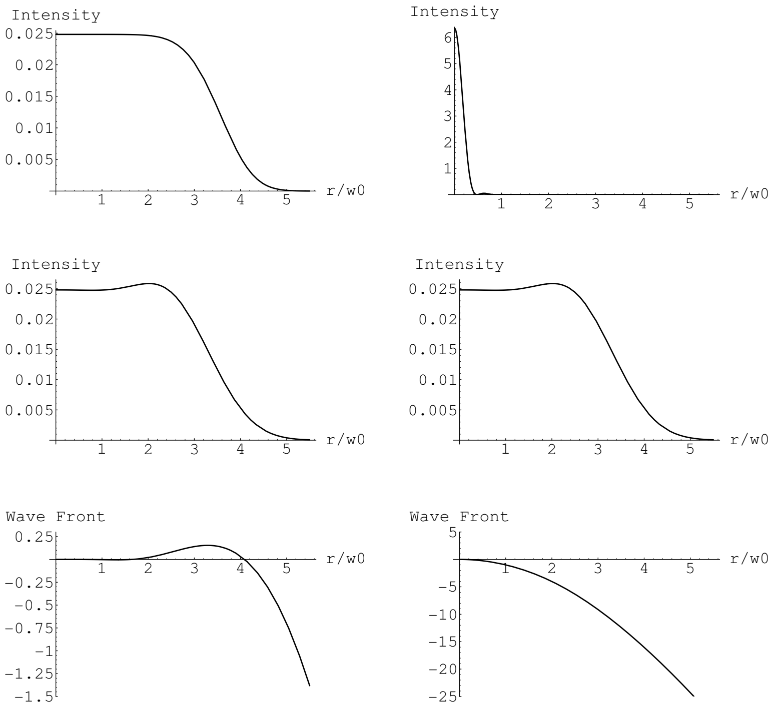

Figure 3.3: Comparison between nearly flat (left panels) and nearly concentric (right panels) Mesa beams. Upper panels: normalized intensity profiles at the center of the cavity. Middle panels: normalized intensity profiles at mirror surfaces Lower panels: phase fronts at the position of the mirrors.

on Eq. (3.58), and obtain

$$\begin{aligned}
& v_{\rm f}^{\rm waist}(r \gg w_0) \\
\approx\ & \frac{1}{\sqrt{\pi}} \int_0^{p/w_0} \sqrt{\frac{x_0}{x}} e^{-(x_0-x)^2} dx_0 \\
\approx\ & \frac{1}{\sqrt{\pi}} \int_{-x}^{p/w_0-x} \left(1+\frac{y}{2x}\right) e^{-y^2} dy \\
\approx\ & \left[\frac{1}{\sqrt{\pi}} \int_{-\infty}^{p/w_0-x} e^{-y^2} dy\right] - \frac{1}{4\sqrt{\pi}x} e^{-(p/w_0-x)^2}\,, \qquad (3.62)
\end{aligned}$$

where we have defined $x \equiv r/w_0$. From Eq. (3.62), we note that when $w_0 \ll r \ll p$, we recover the result of $v_f^{\rm waist} \approx 1$; when r gets close to p, the amplitude will drop, similar to the tail of an error function. Qualitatively, we could write $w_{\text{f-Mesa}}(p) \sim p$. In the ultimate limit of $p/w_0 \to +\infty$, we have

$$v_{\rm f}^{\rm waist}(r) = 1\,, \quad p/w_0 \to +\infty\,. \tag{3.63}$$

The concentric configuration, on the other hand, has a completely different field distribution. According to the analytic expression (3.59), the amplitude must be distributed within a radius of $x \sim w_0/p \ll 1$, or $r \sim w_0^2/p$, which is much smaller than the waist size of the minimal Gaussian. In this case, we could also qualitatively write $w_{\text{c-Mesa}}(p) \sim w_0^2/p$. In the limit of $p \to \infty$, we use

$$\frac{J_1(ax)}{x} \to \delta(x)\,, \quad a \to +\infty \tag{3.64}$$

and have

$$v_{\rm c}^{\rm waist}(r) = \delta(x)\,, \quad p/w_0 \to +\infty\,. \tag{3.65}$$

The fact that

$$w_{\text{f-Mesa}}(p) \cdot w_{\text{c-Mesa}}(p) \sim w_0^2\,, \tag{3.66}$$

clearly reflects the Fourier-transform relation between two Mesa beams with the same p.

Now, let us turn to field distributions at the cavity mirrors. Applying the propagator between parallel planes in the polar coordinate systems (eq. (3.34)),

$$\begin{aligned} &G(r',\phi';r,\phi) \\ &= \frac{ik}{\pi L} e^{-ikL/2} e^{-ik[r^2+r'^2-2rr'\cos(\phi'-\phi)]/L}, \end{aligned} \tag{3.67}$$

we obtain the fields

$$\begin{aligned} v_{\rm f}^{\rm end}(r',\phi') &= \int_0^p r_0 {\rm d}r_0 \int_0^{2\pi} {\rm d}\phi_0 \\ &\quad e^{-\left[\frac{1+i}{2}\right]\left[\frac{r'^2-2r_0r'\cos(\phi'-\phi_0)+r_0^2}{w_0^2}\right]}, \end{aligned} \tag{3.68}$$

$$\begin{aligned} v_{\rm c}^{\rm end}(r',\phi') &= \int_0^p r_0 {\rm d}r_0 \int_0^{2\pi} {\rm d}\phi_0 \\ &\quad e^{-\left[\frac{1+i}{2}\right]\left[\frac{r'^2+2ir_0r'\cos(\phi'-\phi_0)-ir_0^2}{w_0^2}\right]}, \end{aligned} \tag{3.69}$$

at distance $L/2$ from the waist. Comparing Eqs. (3.68) and (3.69), we have

$$\left[v_{\rm f}^{\rm end}(\vec{r})\right]^{*} = e^{ik\vec{r}^{\,2}/L} v_{\rm c}^{\rm end}(\vec{r})\,. \tag{3.70}$$

It is then obvious that the two beams have the same intensity profiles on the cavity mirrors:

$$|v_{\rm f}^{\rm end}(\vec{r})| = |v_{\rm c}^{\rm end}(\vec{r})|\,. \tag{3.71}$$

(An approximate formula for the end-mirror intensity profile was given in the Appendix of [3].) We plot these intensity profiles at the mirror surfaces in the middle panels of Fig. 3.3.

Let us now determine mirror shapes by imposing that the optical phase is constant (which we take as 0 for simplicity) on each mirror surface. We have

$$v_{\rm f}^{\rm end}(\vec{r})e^{ikh_{\rm f}(\vec{r})} = |v_{\rm f}^{\rm end}(\vec{r})|\,, \tag{3.72}$$

$$v_{\rm c}^{\rm end}(\vec{r})e^{ikh_{\rm c}(\vec{r})} = |v_{\rm c}^{\rm end}(\vec{r})|\,. \tag{3.73}$$

Taking the complex conjugate of Eq. (3.72), and combine with Eq. (3.73), using Eqs. (3.70) and (3.71), we have

$$h_{\rm f}(\vec{r}) = \frac{\vec{r}^{\,2}}{L} - h_{\rm c}(\vec{r})\,, \tag{3.74}$$

which is the duality relation between mirror surfaces. In the lower panels of Fig. 3.4, we plot the shapes of mirror surfaces, again, we assume $p = 4w_0$.

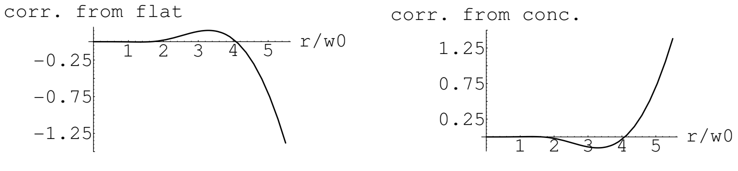

Figure 3.4: Flat mesa beam wave front (left panel) with respect to a flat surface and concentric mesa beam wave front (right panel) with respect to a concentric surface, as analytically computed.

3.4.3 Applications of Mesa beams to Advanced LIGO

In order to achieve lower thermal noise in the test masses, the intensity profiles at the mirrors must be as flat as possible. In the case of infinite mirrors, the choice is to use cavities with flat or concentric spherical mirrors, whose eigenmodes have uniform (absolutely flat) profile distribution. However, the mirrors must have finite sizes (e.g., as limited by the size of the beam tube), and the intensity profiles must be confined to a very large extent within the rims of the mirrors, in order to decrease the diffraction loss upon each reflection. In Advanced LIGO, a power loss below 10 ppm is required [3]. For this reason, we are forced to deviate from flat or concentric configurations — to such an extent that the diffraction loss is within the requirement. When only spherical mirrors are used, if on the one hand we decrease the radius of curvature from $+\infty$ (flat), and on the other hand increase the radius of curvature from $L/2$ (concentric), the dual configurations, with

$$1/(2R_1) + 1/(2R_2) = 1/L\,, \tag{3.75}$$

will have the same intensity profiles at the end mirrors, thus the same diffraction loss and thermal noise. For example, $R_1 = 54\,\mathrm{km}$ and $R_2 = 2.077\,\mathrm{km}$ both give exactly the loss specification, while R_1 is the current baseline design. However, spherical cavities are not optimal in terms of their thermal noise: (the two types of) mesa beams, whose intensity profiles are flatter given the same loss specification, turn out to provide much lower thermal noises [3, 8]. For these beams, the larger the parameter p, the lower the thermal noises, but the higher the diffraction loss. The loss specification of Advanced LIGO corresponds to $p = 4w_0$ [3] which is the case we study in Fig. 3.3.

While having the same diffraction losses and thermal noises, dual configurations do differ significantly in a very important aspect — their eigenspectra are different. Thus, any problem using modal analysis of optical cavities will reveal these differences and probably the duality relation if nearly flat and nearly concentric configurations are compared.

One such problem is the radiation-pressure-induced tilt instability: as the mirrors tilt, the beam inside the cavity walks away from the center of the mirrors, producing a torque, which in some cases can drive more tilt in the same direction, and become destabilizing (see Fig. 3.5). As shown by Sigg [11], while for all cavities there is always one tilt mode in which the radiation-pressure-induced torque is destabilizing, the instability is much weaker

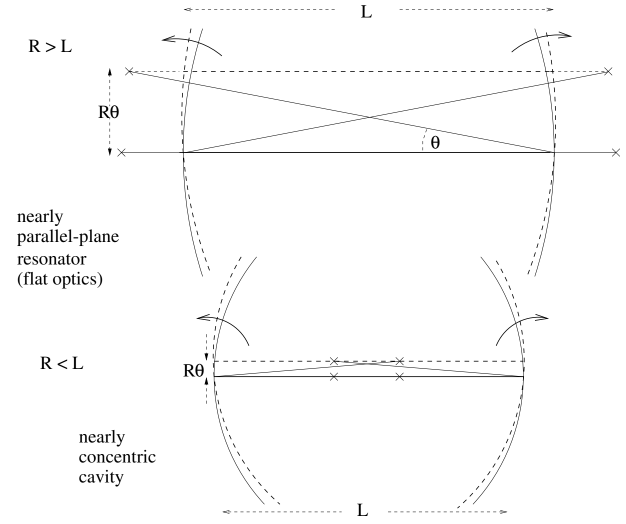

Figure 3.5: Comparison of tilt instability of nearly flat and nearly concentric symmetric optical cavities. For more details see Ref. [10, 11].

in nearly concentric configurations than in nearly flat ones. The reason is that while in the two cases the intensity profiles are identical, the optical axis of the beam walks away by a much smaller distance in the concentric case, given the same amount of tilt in the unstable mode (see Fig. 3.5). According to Sigg's calculation for spherical mirrors, the tilt instability for a nearly flat configuration with Advanced-LIGO power ($\sim 1\,\mathrm{MW}$ circulating in the cavity) can be too strong to handle for the angular control system. For this reason, we would prefer nearly concentric cavities.

For general, non-spherical cavities, a perturbative prescription for calculating the tilt instability has been formulated by Savov and Vyatchanin [10], in which the tilt instability growth time is expressed in terms of eigenvalues and intensity profiles of the cavities' spatial eigenmodes (Eqs. 2.13, 2.14, and 4.8 of [10]). Savov and Vyatchanin applied their prescription to both nearly flat and nearly concentric Mexican-Hat cavities; in particular, they had to solve the eigenvalue problem for the nearly concentric cavities in order to obtain the eigenvalues and intensity profiles. Savov discovered the duality relation in this process. Had the duality relation been known, one could have taken the eigenvalues and intensity profiles of nearly flat Mexican-hat cavities, available from previous works, applied the duality transformation, and obtained the tilt instability for nearly concentric Mexican-Hat cavities without having to solve the eigenvalue problem again (see Section VI of [10]).

Finally, let us make a qualitative comment on the numerical magnitudes of tilt instabilities in the various configurations considered. Numerically, according to Savov and Vyatchanin [10], we have

$$\begin{array}{c}\text{nearly flat MH } (p = 4w_0) \\ \downarrow \\ \text{nearly flat spherical } (R = 54\,\text{km}) \\ \downarrow \\ \text{nearly concentric spherical } (R = 2.077\,\text{km}) \\ \downarrow \\ \text{nearly concentric MH } (p = 4w_0)\end{array}$$

with configurations less and less unstable from top to bottom. Interestingly, this sequence of decreasing instability is consistent qualitatively with the corresponding mirror shapes: with the same amount of diffraction loss, the flat MH does appear more flat than the nearly flat spherical mirrors, while the nearly concentric Mexican-Hat mirror does appear closer to concentric than the nearly concentric spherical mirror.

3.5 Conclusion

In this paper, we provided two different analytic proofs for Savov's duality relation between symmetric cavities with mirror height $h(\vec{r})$ measured with respect to a flat surface and those with mirror height $-h(\vec{r})$ measured with respect to a concentric spherical surface (*valid within the paraxial approximation*): the corresponding eigenmodes have the same intensity profile at the mirrors, their amplitude distribution at the center of the cavity is related via Fourier transform, while their eigenvalues are related by complex conjugation (see Table 3.1). These two proofs are based on the mirror-to-mirror propagator, and the center-to-center propagator, respectively.

We illustrated this duality relation with the two types of Mesa beams proposed for Advanced LIGO. In particular, we showed explicitly that these beams are related to each other by a Fourier transform at the center of the cavities, and that they have the same intensity profiles at the end of the cavities. We also related the mirror shapes of the Mexican-Hat cavities that support these two modes by the duality relation. In addition, the duality relation could have allowed us to avoid solving the eigenequations once more for the nearly concentric Mexican-Hat cavities, and used instead results already available for nearly flat Mexican-Hat cavities.

The duality relation can also be applied to the more general Mesa beams by Bondarescu and Thorne, which interpolate between nearly flat and nearly concentric cavities: in these beams, minimal Gaussians are both translated and have their propagation axes rotated, to different extents [13].

3.6 Appendix A: Duality relation for non-identical mirrors

In this section we will study the duality relation when the mirrors shapes are not identical, but each still symmetric under a 180° rotation around the cavity axis. Since now the field distributions of eigenstates over the two mirror surfaces are not the same, we have to study the eigenvalue problem associated with the round-trip propagator, instead of the individual surface-to-surface ones. Nevertheless, we can still use the propagators (3.6) and (3.8) to build a system of integral equations relating field distributions $v_1(\vec{r}_1)$ and $v_2(\vec{r}_2)$ over the two mirror surfaces. [All through this section, we use the subscripts 1 and 2 to refer to quantities associated with mirrors 1 and 2, respectively.] If the mirrors deviate from parallel planes by $h_{1,2}(\vec{r})$, we have:

$$\gamma_1 v_1(\vec{r}_1) = \int_{S_2} \mathrm{d}^2\vec{r}_2\, \mathcal{K}_{12}(\vec{r}_1,\vec{r}_2)\, v_2(\vec{r}_2)\,, \tag{3.76}$$

$$\gamma_2 v_2(\vec{r}_2) = \int_{S_1} \mathrm{d}^2\vec{r}_1\, \mathcal{K}_{21}(\vec{r}_2,\vec{r}_1)\, v_1(\vec{r}_1)\,, \tag{3.77}$$

where $\gamma_{1,2}$ are the "eigenvalues" and

$$\mathcal{K}_{12}(\vec{r}_1,\vec{r}_2) = \frac{ike^{-ikL}}{2\pi L} e^{ikh_1(\vec{r}_1)-\frac{ik}{2L}|\vec{r}_1-\vec{r}_2|^2+ikh_2(\vec{r}_2)}, \tag{3.78}$$

$$\mathcal{K}_{21}(\vec{r}_2,\vec{r}_1) = \frac{ike^{-ikL}}{2\pi L} e^{ikh_2(\vec{r}_2)-\frac{ik}{2L}|\vec{r}_2-\vec{r}_1|^2+ikh_1(\vec{r}_1)}, \tag{3.79}$$

are the propagators from mirror 2 to mirror 1, and from mirror 1 to mirror 2, respectively. The equations (3.76) and (3.77) give the field at each mirror in terms of the reflected field at the other but they can be combined to form the round-trip equation which states that the field at each mirror must reproduce itself after one round-trip. In the following, we will add a subscript f or c to make a distinction between quantities related to the nearly-flat or nearly-concentric case.

$$\eta_f\, v_{1f}(\vec{r}_1) = \int_{S_1'} \mathrm{d}^2\vec{r}\,'_1\, \mathcal{K}_{1f}^{h_1h_2}(\vec{r}_1,\vec{r}\,'_1)\, v_{1f}(\vec{r}\,'_1), \tag{3.80}$$

$$\eta_f\, v_{2f}(\vec{r}_2) = \int_{S_2'} \mathrm{d}^2\vec{r}\,'_2\, \mathcal{K}_{2f}^{h_2h_1}(\vec{r}_2,\vec{r}\,'_2)\, v_{2f}(\vec{r}\,'_2), \tag{3.81}$$

where the common eigenvalue η_f is given by $\gamma_{1f}\gamma_{2f}$ and the round-trip propagators

$$\begin{aligned}\mathcal{K}_{1f}^{h_1h_2}(\vec{r}_1,\vec{r}\,'_1) &= \int_{S_2} \mathrm{d}^2\vec{r}_2\, \mathcal{K}_{12f}(\vec{r}_1,\vec{r}_2)\, \mathcal{K}_{21f}(\vec{r}_2,\vec{r}_1)\\ \mathcal{K}_{2f}^{h_2h_1}(\vec{r}_2,\vec{r}\,'_2) &= (1\leftrightarrow 2)\cdot \mathcal{K}_{1f}^{h_1h_2}(\vec{r}_1,\vec{r}\,'_1)\end{aligned} \tag{3.82}$$

In the nearly-concentric configuration, using kernels of the form (3.8) for the propagation from one mirror to the other and combining them as done for the nearly-flat configuration, we obtain the following nearly-concentric round-trip equation for the field distribution over the mirror 1 (similar formula for the mirror 2 with the substitution 1 ↔ 2).

$$\eta_c\, v_{1c}(\vec{r}_1) = \int_{S_1'} \mathrm{d}^2\vec{r}\,'_1\, \mathcal{K}_{1c}^{b_1b_2}(\vec{r}_1,\vec{r}\,'_1)\, v_{1c}(\vec{r}\,'_1) \tag{3.83}$$

$$\begin{aligned}\mathcal{K}_{1c}^{b_1b_2}(\vec{r}_1,\vec{r}\,'_1) = -\int_{S_2} \mathrm{d}^2\vec{r}_2\, e^{-2ikL}\left(\frac{k}{2\pi L}\right)^2 \cdot\\ \cdot\, e^{\frac{ik}{2L}|\vec{r}_1+\vec{r}_2|^2+\frac{ik}{2L}|\vec{r}_2+\vec{r}\,'_1|^2+ikb_1(\vec{r}_1)+ikb_1(\vec{r}\,'_1)+2ikb_2(\vec{r}_2)}\end{aligned} \tag{3.84}$$

where $b_{1,2}$ are the mirrors deviations from concentric surfaces. Using the assumed symmetry properties of the mirrors, the propagators for the nearly-flat and nearly-concentric cavity fulfills this relation (the same is true for the mirror 2 with the substitution 1 ↔ 2)

$$\begin{aligned}\mathcal{K}_{1c}^{-h_1-h_2}(\vec{r}_1,\vec{r}\,'_1) &= e^{-4ikL}[\mathcal{K}_{1f}^{h_1h_2}(-\vec{r}_1,-\vec{r}\,'_1)]^*\\ &= e^{-4ikL}[\mathcal{K}_{1f}^{h_1h_2}(\vec{r}_1,\vec{r}\,'_1)]^*\end{aligned} \tag{3.85}$$

Equation (3.85), together with Eqs. (3.82) and (3.83), provides us with a more general duality relation, for cavities with non-identical mirrors: as long as the corresponding mirrors of two cavities A and B satisfy

$$h_{\alpha A}(\vec{r}) = \frac{\vec{r}^{\,2}}{L} - h_{\alpha B}(\vec{r})\,, \quad \alpha = 1,2\,, \tag{3.86}$$

the eigenstates and eigenvalues of the two cavities will be related by:

$$v_{\alpha A} = v^*_{\alpha B}\,, \quad \eta_A = e^{-4ikL}\eta^*_B\,, \quad \alpha = 1, 2\,. \tag{3.87}$$

3.7 Appendix B: Eigenstates and eigenvalues for cavities with infinite mirrors

When the mirrors are infinite, it is straightforward to check that two fundamental properties,

$$\int \mathrm{d}^2\vec{r}\,'\mathcal{K}(\vec{r},\vec{r}\,')\mathcal{K}^*(\vec{r}\,',\vec{r}\,'') \;=\; \delta(\vec{r}-\vec{r}\,'')\,, \tag{3.88}$$

$$\mathcal{K}(\vec{r},\vec{r}\,') \;=\; \mathcal{K}(\vec{r}\,',\vec{r})\,, \tag{3.89}$$

are satisfied by both propagators $\mathcal{K}^h_{\mathrm{f}}$ and $\mathcal{K}^b_{\mathrm{c}}$; they can be re-written into

$$\mathcal{K}\mathcal{K}^\dagger = \mathbf{I}, \quad \mathcal{K} = \mathcal{K}^T\,, \tag{3.90}$$

where $\mathbf{I}$ is identity operator, $\mathcal{K}^T$ the conjugate of $\mathcal{K}$, and $\mathcal{K}^\dagger$ its Hermitian conjugate. In simple terms, $\mathcal{K}$ is unitary and symmetric. It is well known that for unitary operators, all eigenvalues have modulus 1, and that eigenvectors with different eigenvalues are orthogonal to each other.

Now suppose we have an eigenvector v, with eigenvalue γ, $\gamma\gamma^* = 1$. By complex conjugating the eigenequation $\mathcal{K}v = \gamma v$, we obtain

$$\mathcal{K}^* v^* = \gamma^* v^* = \gamma^{-1} v^*\,; \tag{3.91}$$

using Eqs. (3.90), we have $\mathcal{K}^* = \mathcal{K}^\dagger = \mathcal{K}^{-1}$, and hence

$$\mathcal{K}^{-1} v^* = \gamma^* v^* \Rightarrow \gamma v^* = \mathcal{K} v^*\,. \tag{3.92}$$

This means v^* and v are both eigenvectors with eigenvalue γ. We can then replace v and v^* by two real eigenvectors of the eigenvalue problem, $v+v^*$ and $(v-v^*)/i$. This corresponds to the physical fact that the optical phase of eigenstates must be constant on mirror surfaces.

Bibliography

[1] LIGO URL `http://www.ligo.caltech.edu/`.

[2] K. Fritschel, "Laser Interferometer Gravitational Wave Observatory " (2001), URL `http://www.ligo.caltech.edu/docs/T/T010075-00.pdf`.

[3] P. Fritschel, *Second generation instruments for the Laser Interferometer Gravitational-wave Observatory (LIGO), in Gravitational Wave Detection, Proc. SPIE* **4856-39**, p. 282 (2002), URL `gr-qc/0308090`.

[4] K. Thorne, URL `http://www.ligo.caltech.edu/docs/G/G000068-00-D`.

[5] R. O'Shaughnessy, S. Strigin and S. Vyatchanin, Phys. Rev. D, (submitted).

[6] E. d'Ambrosio, R. O'Shaughnessy, S. Strigin, K.Thorne, and S. Vyatchanin, Phys. Rev. D, (submitted).

[7] E. D'Ambrosio, R. O'Shaughnessy, S. Strigin, K. Thorne, and S. Vyatchanin, "Status Report on Mexican-Hat Flat-Topped Beams for Advanced LIGO" (2003) URL `http://www.ligo.caltech.edu/docs/T/T030009-00.pdf`.

[8] J. Agresti and R. DeSalvo," Flat Beam Profile to Depress Thermal Noise", (2005) Aspen Winter Conference, URL `http://www.ligo.caltech.edu/docs/G/G050041-00-Z.pdf`.

[9] The name *mesa beam* is invented by P. Willems.

[10] P. Savov and S. Vyatchanin, "Estimate of Tilt Instability of Mesa-Beam and Gaussian-Beam Modes for Advanced LIGO", Phys. Rev. D**74**, 082002 (2006).

[11] D. Sigg, "Angular Instability in High Power FP Cavities" (2003), URL `http://www.ligo.caltech.edu/docs/T/T030120-00.pdf`.

[12] J. Sidles and D. Sigg, “Optical Torques in Suspended Fabry-Perot Interferometers” (2003) URL `http://www.ligo.caltech.edu/docs/P/P030055-B.pdf`.

[13] M. Bondarescu and K. Thorne, Phys.Rev.D **74**, 082003 (2006).

[14] J.P. Gordon and H. Kogelnik, *The Bell System Technical Journal* Vol.43, pp.2873-2886 (1964) .

[15] A. Siegman, *Lasers*, (Univ. Science Book, 1996),Ch. 19.

[16] A.G.Fox and T.Li ,*The Bell System Technical Journal* Vol.40, pp.453-488 (1961).

[17] H.Kogelnik and T.Li *Applied Optics* Vol.5, N.10 (1966).

Chapter 4

Grid-based search for supermassive black-hole binaries in simulated LISA data

4.1 Introduction

The Laser Interferometer Space Antenna (LISA) is being designed to detect gravitational waves of frequency between 10^{-5} and 10^{-1} Hz, with maximum sensitivity around 10^{-2} Hz. Astrophysical sources in this frequency band are generally split into three broad classes:

1. A rich background of galactic binaries with periods ranging from hours to tens of seconds. This population is mostly dominated by white dwarf binaries.

2. Extreme mass ratio inspirals (EMRIs) consisting of a white dwarf, neutron star or stellar-mass black holes spiraling into a supermassive black hole (mass $\sim 10^5 - 10^7 M_\odot$).

3. Coalescence of SMBH binaries and the capture of intermediate-mass black holes (IMBHs, $\sim 10^2 - 10^4 M_\odot$) by supermassive black holes (SMBHs).

The sources in the third class are the strongest and most promising for LISA. SMBH mergers will be observed with large signal-to-noise ratio (SNR), allowing precise measurements of the source parameters and tests of strong-field effects of general relativity. For that reason, the observation of SMBH mergers is one of the top LISA science requirements.

In view of the wide range of event-rate predictions made by various SMBH binary formation models [2], we could face either of the following two scenarios: (i) Roughly 10

SMBH binary events/year at redshifts (say) $2 < z < 6$; or (ii) hundreds or thousands of SMBH binaries that produce a large (and perhaps stochastic) background in the LISA data. Clearly, the optimal detection strategy to use depends strongly on which of the two scenarios actually occurs in nature; but at this early stage, our best bet is to devise techniques of detection and parameter estimation that encompass both possibilities.

Searches for SMBH binaries in LISA data will be using existing post-Newtonian waveforms [3, 4] to generate the template banks used by the matched-filtering algorithms [5]. Therefore, they will resemble the existing searches for binary-neutron-star(BNS) inspirals in ground-based GW detectors, such as LIGO. However, there are several key differences which are important in choosing the optimal strategy for analyzing the data streams. First, all search methods in LIGO are designed for signals with SNRs $\lesssim 10$, whereas the SNR's of LISA SMBH binaries at distances $z \lesssim 2$ are expected to be hundreds or thousands. Second, the BNS signals sweep through the LIGO frequency band on timescales of order of a few minutes, during which the detector can be considered as unmoving to high accuracy. By contrast, inspirals will dwell in the LISA frequency band for months; and during that time, LISA's velocity and orientation change significantly. That orbital motion will introduce amplitude, frequency and phase modulations of the signal that can be used to determine the SMBH binary's sky location and orientation. Third, as we have already discussed, in the case of LISA, the data will probably contain simultaneous signals from large numbers of SMBH binaries. The challenge is to resolve the individual sources and determine their parameters with high accuracy. Fourth, BNSs observed by ground-based detectors will have become essentially circular by the time they enter the observation band, whereas SMBH binaries may enter the LISA band with considerable eccentricity. Finally, in LIGO the dominant noise originates entirely from the instrument and its surrounding enviroment, while through much of LISA's sensitivity band the dominant noise originates from unresolved Galactic white-dwarf binaries.

As described in Section 1.3, based on the above considerations, our JPL/Caltech group has developed a three-stage search method for SMBH binaries in the Mock LISA Data Challenge (MLDC) data. The goal of our data-analysis pipeline is not only to detect the SMBH signals, but also to provide accurate measurements of the binary parameters. My contribution to this project was to implement the second stage of the pipeline and test it with data from the MLDC. In the rest of this chapter, I will discuss the methodology behind our grid-based search algorithm[1].

The three-stage pipeline, and the grid-based search in particular, are designed to anlyze the MLDC data sets. As such, they are subject to some limitations and approximations. Here is a brief list of these *pseudo*-LISA conventions. Although, one of the goals for the LISA design is to have stationary and Gaussian instrumental noise [1], it will not be clear if this is the case until the instrument is functioning. All data analysis in our work is based on the asumption that the noise is stationary and Gaussian. The LISA orbits are obtained by truncating exact Keplerian orbits for a small mass orbiting the Sun to first order in the eccentricity. LISA noise curves and LISA response are mgenerated with Syntetci LISA [6, 7]. All the massive–black-hole binaries are considered to be circular; black-hole spins are ignored, as are the final plunge and merger phases. An *ad hoc* taper is aplppied at the end of the signal. The injected waveforms are approximated to second post-Newtonian order. The binary is characterized by the folowing parameters: BHs masses m_1, and m_2, time of coalescence t_c, initial angular orbital phase φ_0, ecliptic latitude θ, ecliptic longitude ϕ, polarization angle ψ, orbital inclination ι, and luminosity distance D

The rest of the chapter is organized as follows: In Section 4.2, we introduce the notions of data analysis, optimal filtering, and parameter estimation; In Section 4.3, we derive the F-statistic method which we use to determine the extrinsic parameters of binaries and the coalescence time. Section 4.4 describes details about the numerical implementation of the grid-based search. Lastly, in Section 4.5, we walk the reader through the stages of the the grid-based search. We apply our method to seven different experimental data sets and discuss the results we obtained.

4.2 Parameter estimation

This section briefly reviews the basic formulas behind signal analysis and parameter estimation in the LISA context. For a more complete discussion of this topic see [5] and [8].

The output of each LISA data stream can be written as

$$s_\alpha(t) = h_\alpha(t, \vec{\lambda}) + n_\alpha(t), \tag{4.1}$$

---

[1] We use (perhaps inappropriately) the term "grid-based" to indicate that the search is peformed in the two discretized computational domains (grids) (m_1, m_2) and (θ, ϕ).

where $h_\alpha(t, \vec{\lambda})$ describes the response registered in detector channel α to a source with parameters $\vec{\lambda}$ and $n_\alpha(t)$ denotes the instrument noise in channel α. In the low frequency limit, where the wavelengths are large compared to the armlengths of the detector, the interferometer outputs $s_\alpha(t)$ can be combined to simulate the response of two independent 90 degree interferometers, $s_I(t)$ and $s_{II}(t)$, rotated by 45 degrees with respect to each other [9, 10]. This allows LISA to measure both polarizations of the gravitational wave simultaneously. The third combination of signals in the low frequency limit is insensitive to gravitational waves.

It is often convenient to work with the Fourier transform of the signal.

$$\tilde{s}_\alpha(f) \equiv \int_{-\infty}^{\infty} e^{2\pi i f t} s_\alpha(t)\, dt. \tag{4.2}$$

Under the assumption that the noise is stationary and Gaussian, *Wiener-Khintchine Theorem* [11] implies

$$\langle \tilde{n}_\alpha(f)\, \tilde{n}_\beta(f')^* \rangle = \frac{1}{2}\delta(f - f') S^h_{\alpha\beta}(f), \tag{4.3}$$

where $\langle\ \rangle$ denotes averaging over realizations of the noise, * means complex conjugations, and $S^h_{\alpha\beta}(f)$ is the one-sided spectral density of the noise.

The statistical properties of the noise determine a natural noise-weighted inner product on the vector space of signals. Given two signals $h_1(t)$ and $h_2(t)$, we define $(h_1 \,|\, h_2)$ by

$$(h_1 \,|\, h_2) = 4\,\mathrm{Re} \int_0^{\infty} \frac{\tilde{h}_1(f)^* \tilde{h}_2(f)}{S_n(f)}\, df. \tag{4.4}$$

Based on this definition, the inner product of of pure noise with any signal is a standard random random variable (*i.e.* with normal distribution, zero mean, and unit variance). In particular, the probability for the noise to have some realization n_0 is

$$p(n = n_0) \,\propto\, e^{-(n_0 \,|\, n_0)/2}. \tag{4.5}$$

Therefore, if the actual incident waveform is $h(t)$, then from Eq. (4.1) the probability of measuring a signal s in the detector output is proportional to $e^{-(s-h \,|\, s-h)/2}$. Correspondingly, given a measured signal s, the gravitational waveform h that best fits the data is the one that minimizes the quantity $(s - h \,|\, s - h)$. Eq (4.5) is also reffered to as *likelihood.* Thus, the optimal paramteres that best fits the data is the one that maximizes the likelihood or, the easier to analyze, logarithm of the likelihood. Thus, the alternative names "maximum likelihood"(ML), or "maximum log-likelihood" methods. Another terms we use interchangebly are "optimal filtering" and "matched filtering".

There is a simple geometric interpretation of the opitmal mathcing scenario described above. Let the gravitational signals from coalescing binaries are specified completely by a finite number of parameters λ_i, $i = 1, 2, .., N$. Then the parametrized space of waveforms $\{h(\lambda_i)\}$ is an N-dimensional manifold embedded in the vector space of all possible measured detector outputs s. Given the measured signal $s = n + h(\tilde{\lambda_i})$, where $\tilde{\lambda_i}$ are the true parameters, the best-fit waveform $h(\hat{\lambda_i})$ with optimal (or most probable) parameters $\hat{\lambda_i}$ is the point on the waveform manifold that lies closest to s according to the distance $(s - h(\hat{\lambda_i}) \,|\, s - h(\hat{\lambda_i}))$. Thus, the vector from $h(\hat{\lambda_i})$ to s is then normal to the waveform manifold at $\hat{\lambda_i}$.

It also follows from Eq. (4.4) that for any functions g and k, the expectation value of $(g|n)(k|n)$, for an ensemble of realizations of the detector noise n, is just $(g|k)$. Hence, the signal-to-noise of the detection will be given by

$$\mathrm{SNR[h]} = \frac{(h \,|\, h)}{\mathrm{rms}(h \,|\, n)} = (h \,|\, h)^{1/2}, \tag{4.6}$$

where $\mathrm{rms}(h \,|\, n)$ is the rms value for a n ensemble of realizations of the detector noise, n.

For a given incident GW, different realizations of the noise will give rise to somewhat different best-fit parameters. For large SNR, however, the best-fit parameters will assume a normal distribution centered on the correct values. Specifically, let $\Delta\lambda_i(n) = \hat{\lambda_i}(n) - \tilde{\lambda_i}$ to be the deviation of the best-fit parameters form the true parameters for different realizations of the noise. Then for large SNR the parameter-estimation errors $\Delta\lambda_i$ have the normal distribution

$$p(\Delta\lambda_i) = \mathcal{N}\, e^{-\frac{1}{2}\Gamma_{ij}\Delta\lambda_i\Delta\lambda_j}, \tag{4.7}$$

where Γ_{ij} is the so-called *Fisher information matrix* defined by

$$\Gamma_{ij} \equiv \left(\frac{\partial h}{\partial \lambda_i} \,\middle|\, \frac{\partial h}{\partial \lambda_j} \right), \tag{4.8}$$

and $\mathcal{N} = \sqrt{\det(\Gamma/2\pi)}$ is a normalization factor. For large SNR, the variance–covariance matrix of the errors $\Delta\theta^i$ is given by

$$\langle \Delta\lambda_i \Delta\lambda_j \rangle = (\Gamma^{-1})^{ij} + O(\mathrm{SNR}^{-1}), \tag{4.9}$$

which can be used to determine how accurately one can determine the parameters [12]. Therefore, for large SNRs, the rms errors of the estimated parameters of the signal are given by the square root of the diagonal elements of the inverse of the Fisher information matrix.

4.3 F-Statistic

The F-statistic was originally introduced by Jaranowski, Krolak, and Schutz [13] in the context of ground-based searches by one detector for gravitational wave signals from a known rotating neutron star. Cutler and Schutz [14] generalized the F-statistic to the case of a network of detectors with time-varying noise curves and multiple sources. By using multiple linear filters, the F-statistic allows us to automatically extremize the log likelihood over extrinsic parameters, thus reducing significantly the dimension of the search space.

In the low-frequency limit the LISA response to a gravitational wave with polarization content $h_+(t)$, $h_\times(t)$ can be written as

$$h(t) = h_+(t) F^+(t) + h_\times(t) F^\times(t)\,, \tag{4.10}$$

where

$$\begin{aligned} F^+(t) &= \frac{1}{2}\left(\cos 2\psi\, D^+(t) - \sin 2\psi\, D^\times(t)\right)\,, \\ F^\times(t) &= \frac{1}{2}\left(\sin 2\psi\, D^+(t) + \cos 2\psi\, D^\times(t)\right)\,. \end{aligned} \tag{4.11}$$

The detector pattern functions $D^+(t)$ and $D^\times(t)$ are given in equations (36) and (37) of Ref. [15]. To leading post-Newtonian order a slowly evolving, circular binary has polarization components

$$\begin{aligned} h_+(t) &= A(1+\cos^2\iota)\cos(\Phi(t)+\varphi_0)\,, \\ h_\times(t) &= -2A\cos\iota\,\sin(\Phi(t)+\varphi_0). \end{aligned} \tag{4.12}$$

The gravitational wave phase

$$\Phi(t; f, \theta, \phi) = 2\pi f t + 2\pi f R \sin\theta \cos(2\pi f_m t - \phi), \tag{4.13}$$

couples the sky location and the frequency through the term that depends on the radius of LISA's orbit, $R = 1\text{AU}$, and the orbital modulation frequency, $f_m = 1/\text{year}$.

$$h(t) = \sum_{i=1}^{4} a_i(A, \psi, \iota, \varphi_0) A_i(t; f, \theta, \phi)\,, \tag{4.14}$$

where the time-independent coefficients a_i are given by

$$\begin{aligned}
a_1 &= \frac{A}{2}\left((1+\cos^2\iota)\cos\varphi_0\cos 2\psi - 2\cos\iota\sin\varphi_0\sin 2\psi\right)\,,\\
a_2 &= -\frac{A}{2}\left(2\cos\iota\sin\varphi_0\cos 2\psi + (1+\cos^2\iota)\cos\varphi_0\sin 2\psi\right)\,,\\
a_3 &= -\frac{A}{2}\left(2\cos\iota\cos\varphi_0\sin 2\psi + (1+\cos^2\iota)\sin\varphi_0\cos 2\psi\right)\,,\\
a_4 &= \frac{A}{2}\left((1+\cos^2\iota)\sin\varphi_0\sin 2\psi - 2\cos\iota\cos\varphi_0\cos 2\psi\right)\,,
\end{aligned} \tag{4.15}$$

and the time-dependent functions $A_i(t)$ are given by

$$\begin{aligned}
A_1(t) &= D^{+}(t;\theta,\phi)\cos\Phi(t; f,\theta,\phi),\\
A_2(t) &= D^{\times}(t;\theta,\phi)\cos\Phi(t; f,\theta,\phi),\\
A_3(t) &= D^{+}(t;\theta,\phi)\sin\Phi(t; f,\theta,\phi),\\
A_4(t) &= D^{\times}(t;\theta,\phi)\sin\Phi(t; f,\theta,\phi)\,.
\end{aligned} \tag{4.16}$$

Let also define the 4×4 matrix Γ_{ij} by

$$\Gamma_{ij} = \left(\frac{\partial h}{\partial a_i}\Big|\frac{\partial h}{\partial a_j}\right) = (A_i\,|\,A_j). \tag{4.17}$$

Some times Γ_{ij} is reffered to reduced or projected Fisher information matrix. Given data strem

$$s(t) = h(t) + n(t) = \sum_{i=1}^{4} a_i\, A_i(t) + n(t), \tag{4.18}$$

we want to find the best-fit which mimimizes the deviation from the true signal

$$\delta = \left(s - \sum_i a_i A_i \,\middle|\, s - \sum_j a_j A_j \right) . \tag{4.19}$$

By solving $\partial\delta/\partial a_i = 0$ for the best estimates of the four unknown coefficients $\hat{a_i}$, we obtain the solutions for the unknown coefficients.

$$\begin{aligned} \hat{a_i} &= \sum_k (\Gamma^{-1})_{ik} (A_k \,|\, s); \\ \hat{a_i} &= a_i + \sum_k (\Gamma^{-1})_{ik} (A_k \,|\, n). \end{aligned} \tag{4.20}$$

Substituting (4.14) and (4.20) into Eq. (4.19) we obtain an expression for our optimal statistics

$$\begin{aligned} 2\mathcal{F} &= (s|s) - (s - \sum_i \hat{a_i} A_i \,|\, s - \sum_j \hat{a_j} A_j) \\ &= \sum_{ij} (\Gamma^{-1})_{ij} \, (s \,|\, A_i \,)(s \,|\, A_j). \end{aligned} \tag{4.21}$$

But this is equivallent to maximizing the log lilekihood discussed in the previous section [see Eq. (4.5) and the discussion afterwards.] Therefore, the F-statistic automatically maximizes the log likelihood over the extrinsic parameters A, ι, ψ and φ_0, and reduces the search to the sub-space spanned by f, θ and ϕ.

Note that for SNR $>> 1$, $2\mathcal{F} \approx (\mathrm{SNR})^2$. Whereas, for SNR ≈ 0, (pure noise), $2\mathcal{F} \approx 4$.

The extrinsic parameters can be recovered from the coefficients a_i's via

$$\begin{aligned} A &= \frac{A_+ + \sqrt{A_+^2 - A_\times^2}}{2} , \\ \psi &= \frac{1}{2} \arctan \left(\frac{A_+ a_4 - A_\times a_1}{-(A_\times a_2 + A_+ a_3)} \right) , \\ \iota &= \arccos \left(\frac{-A_\times}{A_+ + \sqrt{A_+^2 - A_\times^2}} \right) , \\ \varphi_0 &= \arctan \left(\frac{c(A_+ a_4 - A_\times a_1)}{-c(A_\times a_2 + A_+ a_3)} \right) , \end{aligned} \tag{4.22}$$

where

$$\begin{aligned} A_+ &= \sqrt{(a_1+a_4)^2+(a_2-a_3)^2}+\sqrt{(a_1-a_4)^2+(a_2+a_3)^2}\,, \\ A_\times &= \sqrt{(a_1+a_4)^2+(a_2-a_3)^2}-\sqrt{(a_1-a_4)^2+(a_2+a_3)^2}\,, \\ c &= \mathrm{sign}(\sin(2\psi))\,. \end{aligned} \tag{4.23}$$

4.4 Numerical implementation

To model the waveforms of the coalescence SMBH binaries, we used SyntheticLISA [6, 7], which was originally developed by Michele Vallisneri in collaboration with John Armstrong. SyntheticLISA generates synthetic time series of the LISA fundamental noises, as filtered through all the Time-Delay Interferometry (TDI) observables. It also computes the data-train output responses to gravitational waves according to a full model of TDI, including the motion of the LISA array and the temporal and directional dependence of the arm-lengths. For detailes of the model underlying SyntheticLISA and the approximations made in generating its data streams, see [first] and the references therein.

To discretize the sky map we used an open-source software package named HEALPix [16] (short for Hierarchical Equal Area isoLatitude Pixelization of a sphere), which was originally devised in 1997 by Krzysztof M. Grski [K.M. Gorski et al., 2005, Ap.J., 622, p.759]. As the name suggests, HEALPix was designed for pixelization, hierarchical indexation, synthesis, analysis, and visualization of data on the sphere. This method of discretization produces a subdivision of spherical surfaces in which each pixel covers the same surface area as every other pixel. The HEALPix grid is characterized by two parameters: N_θ – the number of the base-resolution pixel layers between the north and south poles, and N_ϕ - the number of equatorial, base-resolutions pixels. The total number of pixels is equal to $N_{pix} = N_\theta \times N_\phi$, and the area of each one of them is equal to $4\pi/N_{pix}$. At each level of discretization $l = 2^n$ there are 12×4^n pixels. During our simulations the highest level of discretization we used was $l = 2^{10}$ or more than 12 million pixels.

Our generation of templates is based on a template placement algorithm of Babak *et. al.* [17] and the *findchirp* matched filtering algorithm of Allen *et. al.* [18], both of which were developed for the LIGO binary neutron star searches. Our template-generation algorithm constructs a grid of templates in the (m_1, m_2) computational grid using the metric-based square-grid placement algorithm [19, 17] implemented in the LIGO Algorithm Library (LAL) [20]. The resolution of the grid is specified by its minimum-match parameter MM, which is the minimum overlap between the templates at any point in the parameter space and its nearest grid-point.

The original description of the data sets from the MLDC is: one year of Gaussian stationary instrument noise plus one Schwarzschild SMBH binary with time to coalescence (6±1) months and masses m_1 =(1–5) million solar masses and $m_2 = m_1/x$, where $1 < x < 4$. The signals have SNR for one IFO in the range $450 <$ SNR < 500 . The waveform model for the inspiral is restricted to the 2PN approximation with no spin-orbit nor spin-spin modultations.

For each point in the (m_1, m_2, θ, ϕ), we used the F-statistic method to maximize the log likelihood over the extrinsic parameters A, ι, ψ and φ_0. What is more, we maximize over the coalescence time t_c almost for free. Note, that the expression for the F-statistic Eq. (4.21) contains inner products between the signal and the basis functions A_i Eq. (4.16). However, by definiton Eq. (4.4) the inner products involves Fourier transforms. By numerically performing an inverse Fourier transform we calculate F(t) in the time domain and automatically choose $F(t_c) = F_{max}(t)$.

We ran our simulatons on the JPL Xeon Cluster [21]. This supercomputer cluster has 1052 3.2GHz Intel Pentium 4 processors. It supports parallel programming with the message passing interface (MPI). Each individual run was limited to 12 hours, but most of the time this was enough to execute the search using between 100 and 128 nodes. On average, it took between 50 and 70 seconds to compute one F-statistic.

Most of the code is written in Python. We used mpi4py [22, 23], a software package which provides bindings of the Message Passing Interface (MPI) standard for Python scripting in parallel environments.

4.5 Grid-based search for supermassive black-hole binaries in MLDC data

As described in the previous section, the power of the F-statistic is that it automatically extremizes the log likelihood over the extrinsic parameters of the SMBH binary. In addition it gives us free maximization with respect to the coalescence time t_c. We further try to decouple the dependence of $F = (SNR)^2$ on the remaining four intrinsic parameters (m_1, m_2, θ, ϕ) by observing how strongly F depends on each of the parameters or any combination of them.

First, during our preliminary tests on simultanious searches in the mass grid (m_1, m_2) and the sky-position grid (θ, ϕ)), we realized that the dependence on the sky-position is very weak compared with the dependence on the masses. So in the first step of the search, we fix the sky position to a random point and try to maximize F in the (m_1, m_2) grid. Second, we studied the behavior of $F(\eta, m_c)$, where the symmetric mass ratio η and the chirp mass m_c are defined as follows:

$$\eta = \frac{m_1 m_2}{(m_1 + m_2)^2}, \tag{4.24}$$

$$m_c = (m_1 + m_2)\eta^{3/5}. \tag{4.25}$$

We noticed that F is strongly dependent on the chirp mass and weakly dependent on the symmetric mass ratio. A fact well-known in any post-Newtonian expansions. This allowed us to reduce the first step of the search to an effective one-dimensional optimization of $F(m_c)$ for fixed η. For this purpose, we chose to use a bracketing search method called the *golden ratio search* [24], which effectively narrows the range of the argument inside which the extremum of a function is known to exist.

Since we alreay had access to the JPL supercomputer cluster, instead of maximizing $F(m_c)$ for one value of η we distributed the optimization job to about hundred nodes each with a different value of η. Thus, in one step, we were able to significantly narrow down in the mass grid. This step is very efficient in terms of CPU time. The golden ratio algorithm required between 10 and 15 iterations to reach our desired accuracy. Our targeted accuracy was not very high, because our purpose at this stage was not to detemine the masses of the BHs, but to rapidly converge to a neighbourhood in the (η, m_c) or (m_1, m_2) mass grid, where the sky position becomes important.

In Fig. 4.1 we present the results of our golden-ratio maximization. For each value of η in the range $(0.10, 0.25)$ we plot the maximum value of $F(m_c)$. The plot confirms both our observations: First, the dot near the maximum represents the real values for η and m_c. Although we evaluate F at a random sky position, the values we converge to are very close to the true parameters of the binary. Second, all maxima are concentrated in a

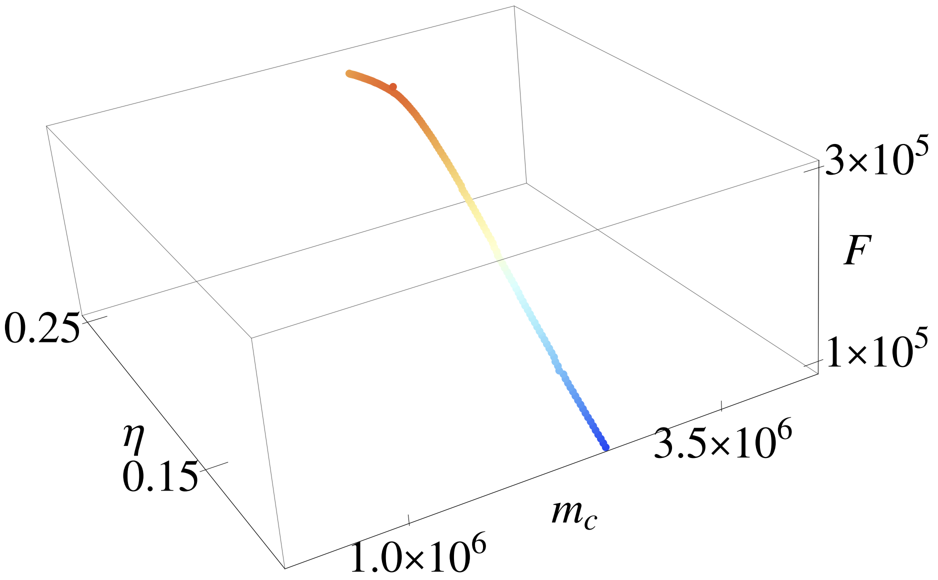

Figure 4.1: Trace of $F_{max}(m_c, \eta)$ for a random sky position. The slightly separated dot near the maximum represents the true values for the masses.

narrow range of η – the trace is almost parallel to the η axis. Figure 4.2 shows the trace of $F_{max}(m_1, m_2)$. Again, the true values of m_1 and m_2 (small dot near the maximum) are close to our convergence point.

After this first step, which required between 10 and 15 minutes of CPU time per node, we were able to converge our guesses for the masses m_1 and m_2 to within less than a percent of the real values. As optimistic as this sounds, it is actually bad news when we turn next to determine the binary's sky position. What this means is that tiny deviations in the masses will produce significant shifts in the optimal sky position, therefore we will need very high accuracy of the two masses in order to have any chance to extract the sky position. The next series of plots demonstrates how weak is the dependence of F on the sky position. Fig. 4.3 was generated at HEALPix level $= 2^7$, with $N_{pix} \approx 2 \times 10^5$ pixels, and area of single pixel $\approx 6 \times 10^{-5}\text{rad}^2$. It took about two days to generate the plot on 100 processors. Although it looks like $F(\theta, \phi)$ is a well-behaved function, the coloring scheme is deceiving. It is extremely non-linear as shown at the bottom of the plot. The three color bars represent: full range of F i.e (F_{min}, F_{max}); 1% range i.e. $(0.99\,F_{max}, F_{max})$; 0.1% range i.e. $(0.999\,F_{max}, F_{max})$. In Fig. 4.4 we show all points on the sky that have F above

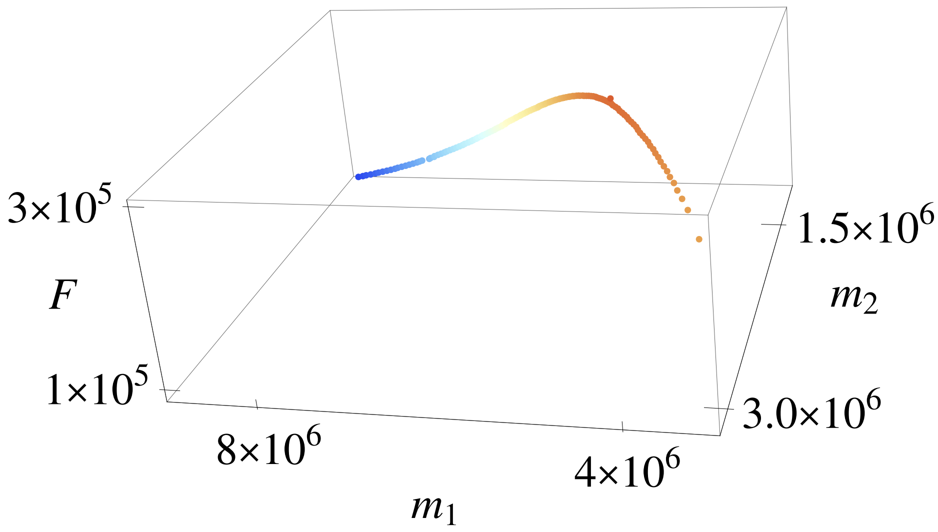

Figure 4.2: Trace of $F_{max}(m_1, m_2)$ for a random sky position. The dot near the maximum represents the true parameters.

$0.999\,F_{max}$. An error of just 0.1% in F translates to uceartanty of tens of degrees in the ecliptic latitude and longitude. Another representation of the data from Fig. 4.3 is shown in Fig. 4.4, where we used linear coloring scheme to emphisize the almost-constant beahviour of F on the sky map.

From the discussion above it is obvious that the resolution of the mass grid (m_1, m_2) must be several orders of magnitude higher that the resolution of the sky grid θ, ϕ. Therefore we start with comperatively coarse sky grid, while keeping the mass grid densly populated.

Another related complication comes from the fact that there is a well-known near degeneracy in the LISA antenna pattern at low frequencies. It is difficult to distinguish between a signal arriving from a certain point in the sky (θ, ϕ) and a signal arriving from the point's antipodal position $(-\theta, \pi \pm \phi)$. As it happened on numerous occasions during the tests, our search almost unpredictably converged to either one of the two *dual* points. We realized that the reason behind this confusion, is in the low mass-grid resolution. The uncertainty in the values of the masses caused an uncertainty in the value of F, which was enough occasionaly to diverge our code to the antipodal point. In Fig. (4.6), we compare F values near the true sky position and its antipodal point. The maximum values near the two points differ

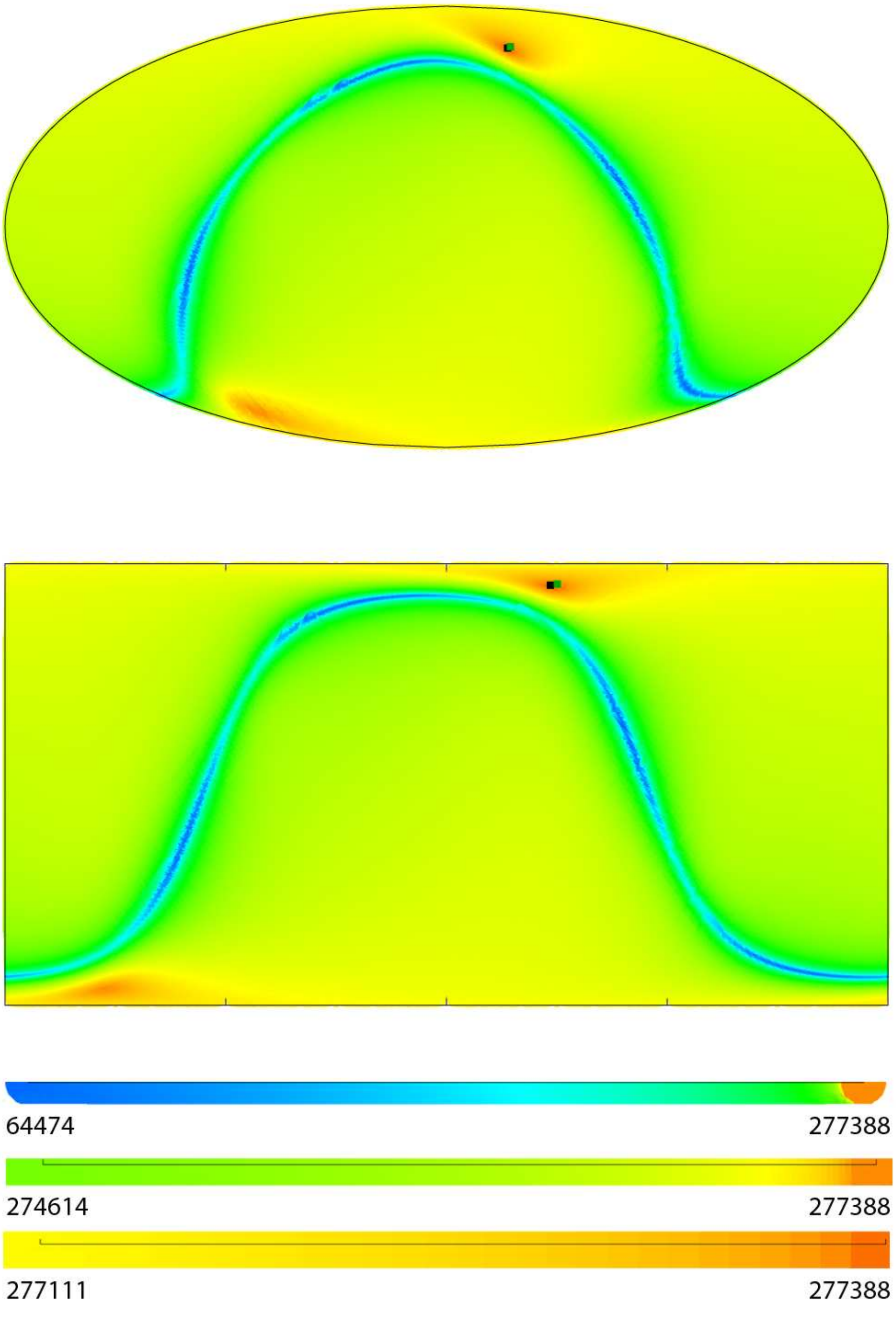

Figure 4.3: $F(\theta, \phi)$ evaluated with best estimates for m_1 and m_2 at each sky point. Upper panel – Mollweide Projection; Lower panel - Lambert Culyndrical Projection. Green dot represents the true sky position and blck dot is sky position determined by grid search. Non-linear coloring schemes for 100%, 1%, and 0.1% intervals.

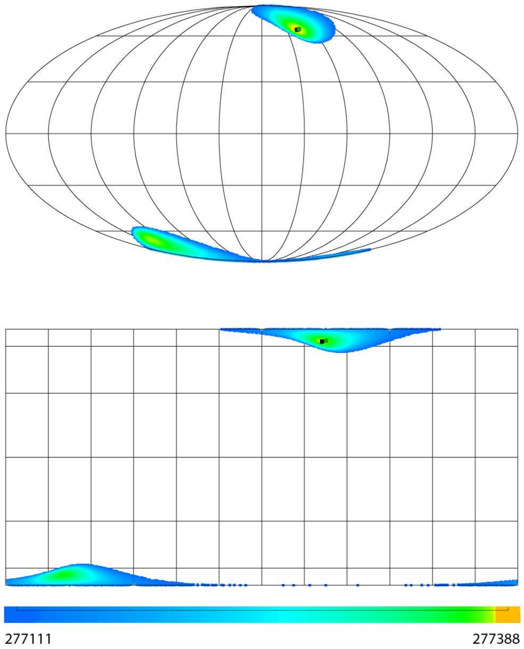

Figure 4.4: Same as Fig. 4.3, but with values of $F(\theta, \phi)$ within 0.1% of F_{max}.

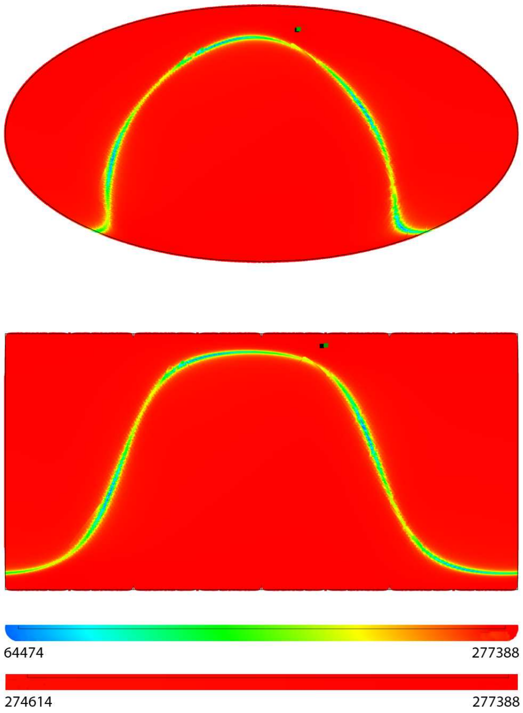

Figure 4.5: Same as Fig. 4.3, but with linear coloring schemes for 100% and 1% intervals.

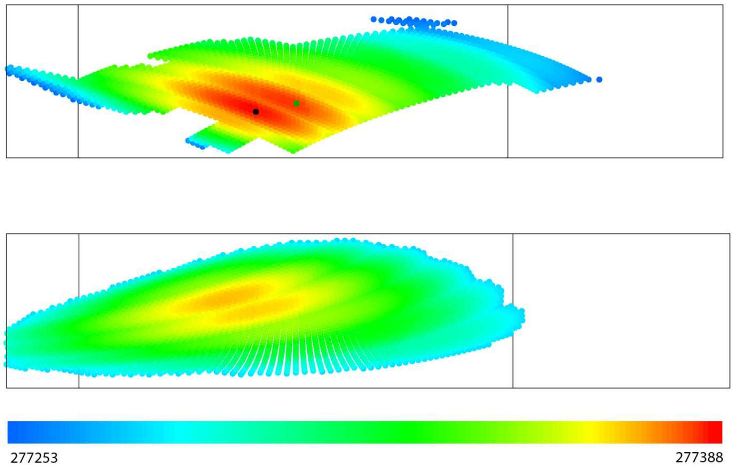

Figure 4.6: $F(\theta, \phi)$ evaluated with true masses m_1 and m_2 near the true sky-position (upper panel) and near the antipodal point (lower panel). Green dot represents the true sky position and black dot is sky position determined by grid search. The sky patch is approximately 30 by 10 degrees.

by 10^{-5}–10^{-4}, depending on the realization of the noise and the sthrength of the signal. Once we improved our mass grid, the code consistently started to converge to the true sky position.

In Fig. (4.6), we also show the best sky position based on our search (black dot) and the true sky position (green dot) for one of the data sets (*Blind).*

[FINSIH DISCUSSION and ADD TABLE w/ Extrinsic Parameters]

Data Set	Parameters	$m1$	$m2$	θ	ϕ	t_c	F_{max}
Training No Noise	key	1204622	401334	0.157	5.998	13636993	379587.1
	search	1204753	401291	0.170	6.001	13636995	379586.6
	key*	1204622	401334	-0.157	9.140	13637969	379537.5
	search*	1204753	401291	-0.170	9.143	13637970	379552.0
Training	key	1204622	401334	0.157	5.998	13636993	380718.7
	search	1204400	401400	0.110	6.062	13636995	380721.8
	key*	1204622	401334	-0.157	9.140	13637969	380660.0
	search*	1204400	401400	-0.110	9.204	13637970	380654.1
Blind	key	4609366	2122425	1.139	3.931	15045889	277384.7
	search	4611146	2121580	1.124	3.900	15045900	277388.4
	key*	4609366	2122425	-1.139	7.073	15045648	277357.8
	search*	4611146	2121580	-1.124	7.042	15045630	277365.9
Exp_1	key	4491973	1235993	-1.340	0.546	16302016	251852.8
	search	4491516	1236333	-1.303	0.531	16301985	251839.4
	key*	4491973	1235993	1.340	3.688	16302211	251849.8
	search*	4491516	1236333	1.303	3.673	16302225	251847.3
Exp_2	key	2996337	1353192	-0.511	0.479	15461667	314489.0
	search	2995151	1353770	-0.507	0.436	15461655	314492.8
	key*	2996337	1353192	0.511	3.621	15462417	314433.0
	search*	2995151	1353770	0.507	3.578	15462420	314435.3
Exp_3	key	3174644	840088	-0.060	5.350	17648966	288204.4
	search	3175067	839993	-0.058	5.338	17648970	288204.0
	key*	3174644	840088	0.060	8.491	17649221	288074.4
	search*	3175067	839993	0.058	8.480	17649210	288071.3
Exp_4	key	2503041	1639502	-0.981	3.185	17485946	449980.7
	search	2502663	1639689	-0.974	3.182	17485950	449980.4
	key*	2503041	1639502	0.981	6.326	17485421	449956.6
	search*	2502663	1639689	0.974	6.324	17485410	449944.8

Table 4.1: Results from grid-based search for seven different data sets. The asterics denote the antipodal position in the sky.

Bibliography

[1] *K. Danzman, et al., LISA – Laser Interferometer Space Antenna, Pre-Phase A Report, Max-Planck-Institute für Quantenoptic, Report MPQ 208 (1996).*

[2] *E. Berti, Class.Quant.Grav.* **23** *785 (2006).*

[3] *K. Arun, L. Blanchet, B. Iyer, and M. Qusailah,* Class. Quant. Grav.**21** *3771 (2004).*

[4] *L. Blanchet, G. Faye, B. Iyer, and B. Joguet,* Phys. Rev. D**65** *061501 (2002).*

[5] *L. Wainstein and V. Zubakov, Extraction of signals from noise (Prentice-Hall, 1996).*

[6] *M. Vallisneri,* Phys. Rev. D **71***, 022001 (2005);*

[7] *Synthetic LISA website, URL* `www.vallis.org/syntheticlisa`.

[8] *C. Cutler and E. Flanagan,* Phys. Rev. D**49***, 2658. (1994)* `arXiv:gr-qc/9402014`.

[9] *C. Cutler, Phys. Rev. D* **57***, 7089 (1998).*

[10] *T. A. Prince, M. Tinto, S. L. Larson & J. W. Armstrong, Phys. Rev. D***66***, 122002 (2002).*

[11] *R. Blandford and K. Thorne,Applications of Clasical Physics (in preparataion), Ch. 5.*

[12] *M. Vallisneri, Phys. Rev. D (submited) (2007),*`arXiv:gr-qc/0703086`.

[13] *P. Jaranowski, A. Krolak, and B. Schutz, Phys. Rev. D* **58** *063001 (1998).*

[14] *C. Cutler and B. Schutz, Phys. Rev. D* **72** *063006 (2005).*

[15] *L. Rubbo, N. Cornish, and O. Poujade, Phys. Rev. D***69** *082003 (2004).*

[16] *HEALPix, URL* `http://healpix.jpl.nasa.gov/`.

[17] *S. Babak, R. Balasubramanian, D. Churches, T. Cokelaer, and B. Sathyaprakash* Class. Quant. Grav.**23** *5477 (2006).*

[18] *B. Allen, W. Anderson, P. Brady D. Brown, and J. Creighton (2005),* `gr-qc/0509116`.

[19] *B. Owen and B. Sathyaprakash,* Phys. Rev. D**60** *022002 (1999).*

[20] *LSC Algorithm Library software packages* LAL *(CVS tag version* `iulgroup_s1_20030420`*),* LALWRAPPER *(version* `iulgroup_s1_20030416`*), and* LALAPPS *(version* `iulgroup-030526`*) were used in this analysis. URL* HTTP://WWW.LSC-GROUP.PHYS.UWM.EDU/LAL

[21] *JPL Dell Xeon cluster, URL* `http://sc.jpl.nasa.gov/hardware/dell1750/`.

[22] *MPI for Python, URL* `http://mpi4py.scipy.org/`.

[23] *mpi4py 0.5.0, URL* `http://pypi.python.org/pypi/mpi4py`.

[24] *W. Press, B. Flannery, S. Teukolsky, and W. Vetterling, Numerical Recipies, (Cambridge Universe Press, 1989).*